Spectral Modeling of Ice-Induced Wave Decay🖉

QINGXIANG LIU

Department of Infrastructure Engineering, University of Melbourne, Melbourne, Victoria, Australia

W. ERICK ROGERS

Naval Research Laboratory, Stennis Space Center, Mississippi

ALEXANDER BABANIN

Department of Infrastructure Engineering, University of Melbourne, Melbourne, Victoria, Australia, and Laboratory for Regional Oceanography and Numerical Modeling, National Laboratory for Marine Science and Technology, Qingdao, China

JIANGKAI LI AND CHANGLONG GUAN

Physical Oceanography Laboratory, Ocean University of China, and Qingdao National Laboratory for Marine Science and Technology, Qingdao, China

ABSTRACT

Three dissipative (two viscoelastic and one viscous) ice models are implemented in the spectral wave model WAVEWATCH III to estimate the ice-induced wave attenuation rate. These models are then explored and intercompared through hindcasts of two field cases: one in the autumn Beaufort Sea in 2015 and the other in the Antarctic marginal ice zone (MIZ) in 2012. The capability of these dissipative models, along with their limitations and applicability to operational forecasts, are analyzed and discussed. The sensitivity of the simulated wave height to different source terms—the ice-induced wave decay S_{ice} and other physical processes S_{other} (e.g., wind input, nonlinear four-wave interactions)—is also investigated. For the Antarctic MIZ experiment, S_{other} is found to be remarkably less than S_{ice} and thus contributes little to the simulated significant wave height H_s. The saturation of dH_s/dx at large wave heights in this case, as reported by a previous study, is well reproduced by the three dissipative ice models with or without the utilization of S_{other} in the ice-infested seas. A clear downward trend in the peak frequency f_p is found as H_s increases. As f_p decreases, the dominant wave components of a wave spectrum will experience reduced damping by sea ice, and finally result in the flattening of dH_s/dx for $H_s > 3$ m in this specific case. Nonetheless, S_{other} should not be disregarded within a more general modeling perspective, as our simulations suggest S_{other} could be comparable to S_{ice} in the Beaufort Sea case where wave and ice conditions are remarkably different.

1. Introduction

Satellite records clearly revealed the decline of the Arctic sea ice extent and thickness over the past several decades (e.g., Maslanik et al. 2011). Contemporary climate models, however, generally fail to capture such rapid loss of the Arctic ice cover (Overland and Wang 2013), indicating that some important physical processes contributing to the sea ice retreat might have been treated too simply or totally neglected. The interaction of ocean surface waves and sea ice is one such important, but often overlooked, phenomenon. A few field experiments in both the Arctic and Antarctic marginal ice zones (MIZs) have demonstrated that energetic wave events could induce fracture and break up of ice pack (e.g., Collins et al. 2015; Kohout et al. 2016), resulting in MIZs more vulnerable to external dynamic and thermodynamic forcing (Williams et al. 2013b; Bennetts et al. 2017). A potential and more effective mechanism that accelerates ice retreat is the positive wave–ice

feedback proposed by Thomson and Rogers (2014) and Squire et al. (2009): the reduction of sea ice cover provides more opportunities for the emerging of energetic waves, and subsequently such waves can cause much more ice break-up and propagate much farther into sea ice. The upward trend of wave heights in the Arctic Ocean, particularly in the Chukchi, Beaufort, and Laptev Seas, has been corroborated by satellite altimeter observations and model reanalysis data (e.g., Liu et al. 2016b; Thomson et al. 2016). Another remarkable evidence of the wave–ice interaction is the formation of pancake ice floes (i.e., small ice plates with raised rims) under agitated wave action during freezing seasons in most of MIZs (e.g., Wadhams 1981).

Two of the primary problems in estimating the impact of waves on sea ice are (i) how much wave energy penetrates into the ice field and (ii) how long this incident wave energy can travel in sea ice. Clearly, to address these problems on a large geophysical scale, we should run a spectral wave model, or even better a fully coupled wave–sea ice model, in which the influences of sea ice on waves, particularly the ice-induced wave decay, should be reasonably parameterized. Attempts to parameterize ice effects into wave models date back to three decades ago, when Masson and Leblond (1989) introduced wave scattering by sparse ice floes into their academic wave model. Later, Perrie and Hu (1996) implemented this scattering scheme into the wave model SWAMP. However, scattering is only effective when the size of ice floes and the wavelengths are comparable, therefore the scattering-based theories cannot perform well in the long wavelength regime, often found in contemporary MIZs (see the two cases analyzed in the present manuscript). As a response to the unprecedented shrinking of the Arctic sea ice since 2007, the research interest in numerical modeling of wave–ice interactions was renewed in the past several years. Numerically, advanced grid systems (e.g., Rogers and Campbell 2009; Li 2012) were designed to extend the applicability of spectral wave models to the polar regions. Physically, several theories pertaining to the ice-induced wave damping and scattering were successively incorporated into wave models (e.g., Rogers and Orzech 2013; Doble and Bidlot 2013) (see an extended discussion about this issue in section 2d).

Among various parameterizations for the ice-induced wave attenuation, the viscoelastic (VE) ice layer model proposed by Wang and Shen (2010, hereafter the WS model) has attracted much attentions in recent years since its implementation in the spectral wave model WAVEWATCH III (Rogers and Zieger 2014; Cheng et al. 2017). Li et al. (2015) and Rogers et al. (2016) have demonstrated that the WS model was capable of fitting field measurements of the total energy (in terms of the significant wave height H_s) of ice-coupled waves. Nonetheless, having identified the drawback of the numerical solver for the WS model, Mosig et al. (2015) proposed two alternative, mathematically simpler VE beam models, making good candidates for implementation in spectral wave models. The first beam model extends the purely elastic plate model of Fox and Squire (1994) by taking a complex elastic modulus of the ice layer and by restricting it to two dimensions. Hereafter, we will refer to it as the extended Fox and Squire (EFS) model. The second beam model, first derived by Robinson and Palmer (1990), considers the ice-induced wave damping to be dependent on the vertical velocity of the ice layer (hereafter the RP model). In this study, we first implemented the two VE beam models, together with another viscous model proposed by Meylan et al. (2018, their section 6.2), which assumes the loss of wave energy is proportional to the horizontal ice velocity squared times the ice thickness (hereafter the M2 model), into the third generation (3G) spectral wave model WAVEWATCH III (hereafter WW3; WW3DG 2019) and then explored the performance of these models in two case studies.

The paper is organized as follows. We first present a brief review of previous works on wave–ice interactions in section 2, particularly from a numerical wave modeling perspective. The details of the three selected sea ice models (EFS, RP, and M2) and their implementations in WW3 are described in section 3. In section 4, we then applied WW3 with these attenuation models to two case studies, including hindcasts of ice-coupled wave fields in the autumn Beaufort Sea in 2015 and in the Antarctic MIZ in 2012. Model simulations are compared with in situ buoy measurements in section 5, followed by discussions in section 6 on (i) the sensitivity of the simulated wave height to different source terms [i.e., the ice-induced wave decay and other physical processes such as wind input (e.g., Donelan et al. 2006) and nonlinear four-wave interactions (Hasselmann 1962)], (ii) further intercomparisons of the three ice models, and (iii) the applicability of these models to operational forecasts. A brief conclusion in section 7 finalizes this paper.

2. Previous works on wave–ice interactions

a. Spectral wave modeling in ice-free waters

WW3 solves the radiative transfer equation (RTE) to predict the generation, evolution, and dissipation of ocean surface waves. When currents and ice are *absent*, the deep-water RTE is generally written as follows (e.g., Holthuijsen 2007):

$$\frac{\partial N}{\partial t} + \nabla \cdot \mathbf{c}_g N = \frac{S_T}{\omega}, \qquad (1)$$

$$S_T = S_{in} + S_{ds} + S_{nl} + \cdots, \qquad (2)$$

where $N(\omega, \theta; \mathbf{x}, t) = F(\omega, \theta; \mathbf{x}, t)/\omega$ is the wave action density spectrum, $F(\omega, \theta; \mathbf{x}, t)$ is the frequency-direction spectrum, ω is the intrinsic (radian) frequency, and $\mathbf{c}_g$ is the (intrinsic) group velocity. The terms in the LHS of (1) signify kinematic change of wave spectrum. The radian frequency ω is related to the wavenumber k through the following linear wave dispersion relation

$$\omega^2 = gk, \qquad (3)$$

where g is the gravitational acceleration. The source terms (S_T) in the RHS of (1) characterize dynamic changes of wave energy due to different physical processes [(2)], including the generation of ocean waves by wind (S_{in}; e.g., Donelan et al. 2006), dissipation induced by wave breaking (S_{ds}; e.g., Babanin 2011), and redistribution of energy over the spectral space as a result of the nonlinear four-wave resonant interaction (S_{nl}; Hasselmann 1962). The reader is referred to Young (1999) and Holthuijsen (2007) for thorough reviews of these topics.

b. Ice effects on waves

Field experiments and theoretical analyses suggested that ocean waves impinging on ice floes or ice packs would experience noticeable kinematic and dynamic changes. First, wave energy decays exponentially with distance (e.g., Wadhams et al. 1986), according to an equation of the form

$$\frac{1}{F(f,x)} \frac{dF(f,x)}{dx} = -\alpha_a(f, \mathscr{T}), \qquad (4)$$

where $F(f, x)$ is the one-dimensional wave spectrum at a penetration x, α_a (m^{-1}) is the *apparent* spatial attenuation rate of wave energy, which depends on wave frequency f and ice parameters $\mathscr{T}$, for example, ice type, floe size, thickness, viscosity. Under the same ice conditions, α_a generally decreases with increasing wave period T; therefore ice behaves as a low-pass filter for the incident wave components (see, e.g., Fig. 3 of Collins et al. 2015). A consequence of such frequency filtering is the downshifting of the spectral peak as waves penetrate into ice fields (Sutherland and Gascard 2016).

Second, the dispersion relation for ice-coupled waves may deviate from that for open-water waves [Eq. (3)], particularly for high-frequency components (Sutherland and Rabault 2016; Collins et al. 2018). Accordingly, the wavelength will be shortened or lengthened, depending on the type of sea ice that waves are interacting with (Collins et al. 2016). It should be mentioned, however, that the concept of wavelength in the MIZ is not as clear

as in the open water because of the inhomogeneity of the MIZ medium.

Third, the directional properties of wave fields are also modified by sea ice. A consistent picture of this phenomenon is short waves broaden quickly due to scattering and may spread to isotropy very near the ice edge [say, within $\mathscr{O}(1)$ km of the edge], whereas dissipation dominates for long waves likely causing directional narrowing (e.g., Wadhams et al. 1986; Sutherland and Gascard 2016; Squire and Montiel 2016; Montiel et al. 2018).

c. Introducing ice effects into RTE

It was first suggested by Masson and Leblond (1989) that the RHS of the RTE in (2) could be rewritten as follows to take ice effects into account

$$S_T = (1 - C_I)(S_{in} + S_{ds}) + S_{nl} + C_I S_{ice} + \cdots, \qquad (5)$$

where S_{ice} is the new term added to parameterize the dynamic impacts of sea ice on waves (i.e., attenuation and spreading) and C_I is the ice concentration. Both wind input and wave breaking terms (S_{in} and S_{ds}) are reduced by a factor $(1 - C_I)$ as it is assumed that "waves can neither be generated by wind nor dissipated by the usual breaking mechanism in that fraction C_I of the sea surface covered by ice" (Masson and Leblond 1989). The nonlinear four-wave interaction S_{nl}, however, is left unchanged (see also Polnikov and Lavrenov 2007). Although these ad hoc assumptions were not evidence-based, the scaling of ice-free source terms in (5) has been followed by a number of studies for lack of an alternative (e.g., Perrie and Hu 1996; Rogers et al. 2016).

Due to the complexity of the interaction of ocean waves and sea ice, the parameterization of S_{ice} is rather diverse in the literature. As reviewed by Squire et al. (1995) and Squire (2007, 2020), the ice-induced wave damping mainly results from

(i) the conservative scattering process by the highly dynamic and heterogeneous ice terrain and morphology. Wave energy incident on finite solitary floes is partly reflected and partly transmitted. As waves propagate into the ice farther, the cumulative partial-transmission effects by multiple floe edges directly contribute to the exponential decay of the *forward-going* wave energy (e.g., Kohout and Meylan 2008; Montiel et al. 2016).

(ii) the dissipative processes such as viscous effects existing in the ice layer and its underlying wave–ice boundary layer (e.g., Liu et al. 1991; Keller 1998; Wang and Shen 2010; Voermans et al. 2019; Rabault et al. 2019), overwash near the floe's front (Skene et al. 2015; Toffoli et al. 2015), wave-driven floe collisions

and breakup (e.g., Collins et al. 2015), etc. It is noteworthy that the dissipation mechanism closely depends on the ice type (e.g., grease/pancake ice, ice floe, and continuous ice).

It should be highlighted that these two distinct mechanisms, that is, scattering and dissipation, have different implications on the directionality of the wave spectrum. The scattering mechanism redistributes wave energy in all directions and therefore broadens the directional spectra, whereas the dissipation mechanism narrows the spectra due to the pathlength effect. Wadhams et al. (1986, their section 6) provided an excellent qualitative explanation for how these two mechanisms combine together in determining the directional spreading of wave fields. However, a quantitative description of the relative precedence of scattering and dissipation remains largely unexplored [with a few exceptions, e.g., Ardhuin et al. (2016) and Montiel et al. (2018)]. It is generally accepted that dissipation dominates over scattering at low frequencies as wavelengths of such wave modes are much longer than the floe size—a typical situation where scattering becomes less effective (e.g., Kohout and Meylan 2008).

Based on the abovementioned, the most reasonable parameterization of S_{ice} may be (Meylan and Masson 2006)

$$S_{\text{ice}} = \mathscr{B}_\vartheta S_{\text{ice}}^\vartheta + \mathscr{B}_s S_{\text{ice}}^s + \mathscr{B}_d S_{\text{ice}}^d, \tag{6}$$

$$S_{\text{ice}}^\vartheta(\omega, \theta; \mathbf{x}, t) = c_g \int_0^{2\pi} \mathscr{S}_{\mathscr{K}}(\omega, \theta, \vartheta; \mathbf{x}, t) F(\omega, \vartheta; \mathbf{x}, t)\, d\vartheta, \tag{7}$$

$$S_{\text{ice}}^s(\omega, \theta; \mathbf{x}, t) = -c_g \alpha_s(\omega, \theta; \mathbf{x}, t) F(\omega, \theta; \mathbf{x}, t), \quad \text{and} \tag{8}$$

$$S_{\text{ice}}^d(\omega, \theta; \mathbf{x}, t) = -c_g \alpha_d(\omega, \theta; \mathbf{x}, t) F(\omega, \theta; \mathbf{x}, t), \tag{9}$$

where S_{ice} is split into three parts: wave amplification due to scattering of wave components incident along the ϑ direction ($S_{\text{ice}}^\vartheta; \vartheta \neq 0$), wave attenuation due to scattering of the wave component incident in the θ direction (S_{ice}^s), and wave attenuation caused by dissipative processes (S_{ice}^d). The term $\mathscr{S}_{\mathscr{K}}(\omega, \theta, \vartheta; \mathbf{x}, t)$ in (7) is the so-called scattering kernel that specifies wave energy redirected in the θ direction for a wave incident in the ϑ direction (Meylan and Masson 2006). Determining the scattering-induced attenuation rate α_s in (8) and the scattering kernel $\mathscr{S}_{\mathscr{K}}$ requires the development of two-dimensional or three-dimensional scattering models (e.g., Kohout and Meylan 2008; Montiel et al. 2016; Zhao and Shen 2016). A number of viscous theories have been proposed to estimate the dissipation-related attenuation rate α_d in (9) (e.g., Robinson and Palmer 1990; Keller 1998; Wang and Shen 2010; Mosig et al.

2015). In (6), the binary parameters $\mathscr{B}_\vartheta$, $\mathscr{B}_s$, and $\mathscr{B}_d$ are introduced to control whether the respective terms are switched on (i.e., $\mathscr{B} = 1$) or not (i.e., $\mathscr{B} = 0$). It is worth mentioning that S_{ice}^ϑ is primarily responsible for redistributing wave energy in all directions as a result of scattering. It is expected that, in the scattering-dominant regime, the spreading effect by sea ice could not be simulated properly if S_{ice}^ϑ is neglected (i.e., $\mathscr{B}_\vartheta = 0$).

d. Previous studies on parameterizations of S_{ice}

Previous works on the parameterization of S_{ice} in the spectral wave models and wave–ice interaction models are summarized in Table 1. What we can learn from these pioneering works are (i) that it is the practice of prior researchers to ignore S_{ice}^ϑ when directional information of waves is unavailable or when scattering is thought to be unimportant (e.g., Doble and Bidlot 2013; Rogers et al. 2016); (ii) that the scattering theory (S_{ice}^s with/without S_{ice}^ϑ) alone tends to underpredict the attenuation of long waves and thus complementary dissipative terms (S_{ice}^d) must be added (e.g., Kohout and Meylan 2008; Williams et al. 2013a, 2017); and (iii) that under certain ice conditions, some standalone dissipative parameterizations (S_{ice}^d) (e.g., Liu et al. 1991; De Carolis and Desiderio 2002; Mosig et al. 2015; Rabault et al. 2019) have been demonstrated to fit reasonably well the observed apparent attenuation rates α_a resulting from the collective effect of all the attenuation mechanisms. Finally, previous works generally chose the ice-free $\mathbf{c}_g$ to advect wave energy by assuming that the ice-induced change in $\mathbf{c}_g$ is not significant, at least for long waves (e.g., Dumont et al. 2011; Williams et al. 2013a). Although this is far from settled, recent wave measurements in ice suggest such assumption appears reasonable. Sutherland and Rabault (2016) showed that in landfast ice, the linear open-water dispersion relation (3) holds up to 0.12 Hz (wave period greater than 8 s). Collins et al. (2018) found observations in a mixture of pancake ice and frazil ice nearly exactly coincide with (3) for the frequency range 0.1–0.3 Hz (wave period 3–10 s).

3. Estimation of attenuation rates α_d

Putting the ice-induced wave scattering aside, we focus on the dissipation-related parameterizations only in this study (i.e., $\mathscr{B}_\vartheta = \mathscr{B}_s = 0$). Consequently, (6)–(9) are simplified as

$$S_{\text{ice}} = S_{\text{ice}}^d = -c_{g0}\alpha_d(\omega; \mathbf{x}, t) F(\omega, \theta; \mathbf{x}, t), \tag{10}$$

where c_{g0} highlights the ice-free group velocity we adopt. As mentioned in section 1, three ice models are chosen for estimating α_d. Each of the two VE models

TABLE 1. Previous works on the parameterization of S_{ice} (S_{ice}^θ, S_{ice}^s, S_{ice}^d) in wave and ice models and the corresponding theories. The required ice properties for each study are also listed, such as the ice concentration C_i, ice thickness h_i, elastic shear modulus of ice layer G, viscosity parameter η, etc. See the table footnotes for more details.

Study	S_{ice}^θ	S_{ice}^s	S_{ice}^d	Ice properties[a]
Masson and Leblond (1989) and Perrie and Hu (1996)	Masson and Leblond (1989)	Masson and Leblond (1989)	Masson and Leblond (1989)[b]	C_i, h_i, D_F, η
Meylan et al. (1997)[c]	Meylan and Squire (1996)	Meylan and Squire (1996)	Meylan et al. (1997)[b]	C_i, h_i, D_F, η
Dumont et al. (2011)[c]	—[d]	Kohout and Meylan (2008)	—	C_i, h_i, D_F
Doble and Bidlot (2013)	—	Kohout and Meylan (2008)	Kohout et al. (2011)	C_i, D_F, η
Williams et al. (2013a)[c]	—	Bennetts and Squire (2012)	Robinson and Palmer (1990)	C_i, h_i, D_F, η
Rogers and Orzech (2013)	—		Liu and Mollo-Christensen (1988)	C_i, h_i, η
Rogers and Zieger (2014) and Rogers et al. (2016)	—		Wang and Shen (2010)	C_i, h_i, G, η
Boutin et al. (2018)[e]	Meylan and Masson (2006)	Bennetts and Squire (2012)	Wadhams (1973), Liu and Mollo-Christensen (1988), and Boutin et al. (2018)	C_i, h_i, D_F, C_P

[a] For simplicity, we use D_F to represent all the floe size-related parameters. Similarly, η is used to denote all the dissipative/viscous parameters in different dissipative models. The term C_P in the last cell signifies all the parameters used in the anelastic and inelastic attenuation terms described in Boutin et al. (2018).

[b] Masson and Leblond (1989) and Meylan et al. (1997) used a frequency-independent dissipation-related attenuation rate α_d.

[c] Other source terms listed in the RTE (5) (S_{in}, S_{ds}, S_{nl}) were not considered in these studies.

[d] A dash (—) indicates not applicable.

[e] The scattering kernel used in Boutin et al. (2018) is frequency-dependent but isotropically distributed $\mathscr{S}_{\mathscr{K}}(\omega) = \alpha_s(\omega)/2\pi$.

(EFS and RP) describes the infinitely long, floating ice layer as a homogeneous viscoelastic medium, the characteristics of which are represented by two *empirical* rheological parameters, namely the elastic shear modulus of the ice layer G and the viscosity of the ice layer η. Under this paradigm, the dispersion relation is modified as (Mosig et al. 2015)

$$Qg\kappa \tanh(\kappa d) - \omega^2 = 0, \tag{11}$$

where d is the water depth and $\kappa = k_r + ik_i$ is the complex wavenumber of ice-coupled waves. The real part $k_r = 2\pi/\lambda$ characterizes the effect of ice on the wavelength and $k_i = \alpha_d/2$ is the attenuation rate of wave amplitude. The Q term in (11) for the EFS and RP models reads

$$Q_{\mathrm{EFS}} = \frac{G_\eta h_i^3}{6\rho_w g}(1+\nu)\kappa^4 - \frac{\rho_i h_i \omega^2}{\rho_w g} + 1, \tag{12}$$

$$Q_{\mathrm{RP}} = \frac{G h_i^3}{6\rho_w g}(1+\nu)\kappa^4 - \frac{\rho_i h_i \omega^2}{\rho_w g} + 1 - i\frac{\omega\eta}{\rho_w g}. \tag{13}$$

Here ρ_w (ρ_i) is the density of water (sea ice), h_i is the ice cover thickness, $G_\eta = G - iw\rho_i\eta$ is the complex shear modulus, and $\nu \simeq 0.3$ is the Poisson ratio of sea ice (Mosig et al. 2015). The viscosity parameter η for the EFS model has the dimension of the kinematic viscosity ($\mathrm{m^2\,s^{-1}}$), whereas η for the RP model denotes a constant viscous damping force per unit area and per unit velocity ($\mathrm{kg\,m^{-2}\,s^{-1}}$; Meylan et al. 2018). Due to their high similarity, (12) and (13) can be computed by a single solver. We implemented these two models into WW3 as IC5 (WW3DG 2019) and solved the dispersion relations (11)–(13) iteratively using the Newton–Raphson method (see appendix).

Through a detailed theoretical analysis, Meylan et al. (2018) suggested under the assumption that k_r does not deviate from the open-water wavenumber k_0 significantly, and that the attenuation rate k_i is weak, the two VE models described above predict

$$k_i^{\mathrm{EFS}} \simeq \eta h_i^3 \omega^{11}, \tag{14}$$

$$k_i^{\mathrm{RP}} \approx \frac{\eta}{\rho_w g^2} \omega^3, \tag{15}$$

whereas previous field measurements (e.g., Meylan et al. 2014; Cheng et al. 2017) support a power law $k_i \propto \omega^n$, with n between 2 and 4. Equations (14) and (15) indicate at certain regimes (i.e., $k_r \approx k_0$ and low k_i), k_i of the EFS model is too sensitive to wave frequency and k_i of the RP model shows no dependence on ice thickness.
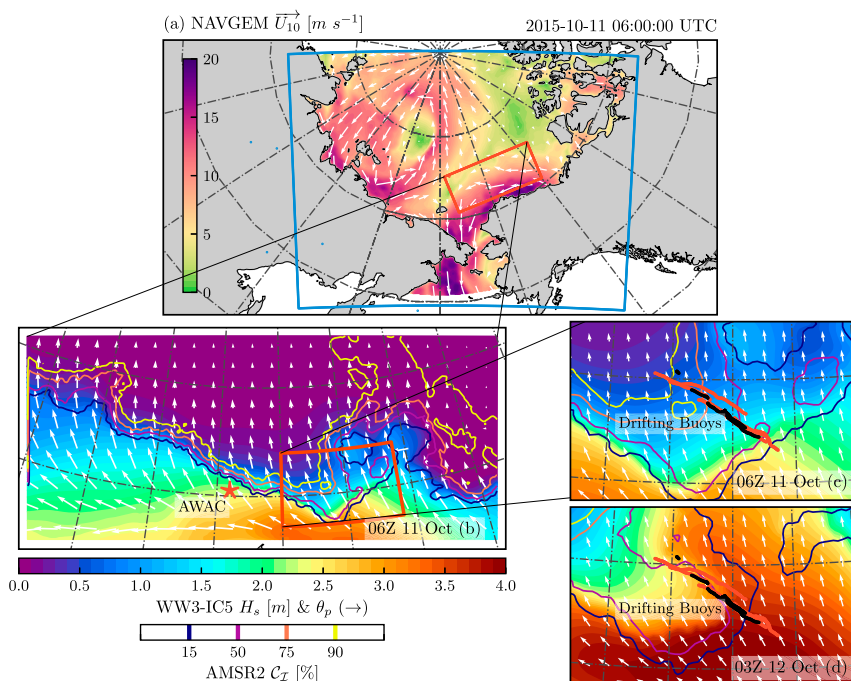
FIG. 1. (a) A snapshot of wind forcing $\mathbf{U}_{10}$ (shaded contour: wind speed; white arrows: wind direction) from the atmospheric model NAVGEM at 0600 UTC 11 Oct 2015. The blue (red) box outlines the 10-km G01 (5-km G02) curvilinear grid used for the WW3 model. (b) Wave fields in the inner grid (G02) as simulated by WW3-M2 model (shaded contour: H_s; white arrows: peak wave direction θ_p). The red star marks the moored subsurface AWAC (Nortek Acoustic Wave and Current) buoy. (c) A zoomed-in view of the study area with red (black) dots highlighting the trajectories of the SWIFT (U.K.) drifting buoys. (d) As in (c), but for 0300 UTC 12 Oct 2015. The AMSR2 ice concentration data C_I are shown as colored contour lines in (b)–(d).

Assuming the change in wavelength is small, Meylan et al. (2018) further proposed the M2 model, given by

$$k_i^{M2} = \frac{\eta h_i}{\rho_w g^2} \omega^3, \qquad (16)$$

where k_i is linearly scaled with h_i, similar to the field measurements collected in Doble et al. (2015) under pancake ice and η is in kilograms per cubic meter per second (kg m^{-3} s^{-1}). Following the suggestion of Meylan et al. (2018) that the M2 model "is likely to be more widely applicable" than the RP model because of its dependence on h_i, we also implemented the M2 model in the framework of IC5 (WW3DG 2019).

4. Numerical simulations of waves in ice

In this section, we describe two cases designed to evaluate the performance of three different attenuation models implemented in WW3. One is the hindcast of waves in the autumn Beaufort Sea in 2015, and the other is the modeling of waves in the Antarctic MIZ in 2012. Details of these two cases are presented in sections 4a and 4b, respectively.

a. R/V Sikuliaq cruise 2015

The 6-week cruise on the ice-capable research vessel R/V Sikuliaq, conducted over the period from 30 September to 9 November 2015, has provided wave and ice measurements in the Chukchi and Beaufort Seas (Thomson et al. 2018). Same as Rogers et al. (2016), we focus on an energetic wave event during 11–14 October 2015. Within this period, a stormy system prevailed in the southwestern Beaufort Sea, generating strong easterly and southeasterly winds ($U_{10} \gtrsim 15$ m s^{-1}) and waves (H_s) up to 4 m surrounding Sikuliaq (Figs. 1a,d).

A large array of drifting wave buoys (red and black dots in Fig. 1c) was deployed to measure wave penetration into the ice edge, including six Surface Wave Instrument Float with Tracking (SWIFT) buoys (Thomson 2012) and five U.K. wave buoys (Wadhams and Thomson 2015). It has been found, however, the SWIFT and U.K. buoy systems were not fully consistent as H_s from the former was on average 0.7 m lower than that from the latter [section S1 in the online supplemental material; see also Montiel et al. (2018)]. We have used the

TABLE 2. Numerical setup of WW3 for the two cases, including the model domains, grid resolutions (Δx), frequency and direction grids ($f_i = f_1 \times 1.1^{i-1}$, $i = 1, \ldots, N_f$, $\Delta\theta = 10°$, $N_\theta = 36$), time steps (the global time step Δt_g, time steps for spatial advection Δt_x, intraspectral propagation Δt_f, and the integration of source terms Δt_s; see WW3DG 2019), wind forcing $\mathbf{U}_{10}$, ice concentration C_I, ice thickness h_i, and the simulation periods. The tuning parameter β_{max}, controlling the strength of S_{in} from Ardhuin et al. (2010), is also presented here.

Model attributes	R/V *Sikuliaq*, 2015	SIPEX II, 2012
Grid	G01: blue box in Fig. 1a ($\Delta x \sim 10$ km)	100°–150°E, 75°–45°S ($\Delta x = 0.25°$)
	G02: red box in Fig. 1a ($\Delta x \sim 5$ km)	
f_1, N_f	$f_1 = 0.045$ Hz, $N_f = 30$	$f_1 = 0.0373$ Hz, $N_f = 35$
Δt_g, Δt_x, Δt_f, Δt_s	G01: 900, 450, 450, 50 s	600, 300, 300, 60 s
	G02: 900, 225, 450, 25 s	
$\mathbf{U}_{10}$	NAVGEM (0.5°, 3 hourly; Hogan et al. 2014)	CFSv2 ($\sim$0.2°, hourly; Saha et al. 2014)
C_I	G01: AMSR2 (3.125 km, daily)[a]	SSM/I (12.5 km, daily; Kaleschke and Kern 2006)
	G02: AMSR2 (10 km, $\sim$5.3 hourly)[b]	
h_i	0.15 m	0.75 m
β_{max}	1.1	1.0
Simulation period	1–15 Oct 2015	16 Sep–10 Oct 2012

[a] The 3.125-km, daily AMSR2 ice concentration data were sourced from Beitsch et al. (2014) and Kaleschke and Tian-Kunze (2016).
[b] The 10-km, $\sim$5.3-hourly AMSR2 swath data were provided by Dr. Li Li (U.S. Naval Research Laboratory).

SWIFT observations only in the following analysis simply because (i) the sampling size of SWIFT observations is remarkably larger ($N = 497$ versus $N = 254$, where N is the total number of the available buoy records), and (ii) the best agreement between SWIFT records and WW3 simulations that we can achieve is relatively better than that for U.K. records. The whole data duration spans from 0100 UTC 11 October to 2200 UTC 14 October 2015. Both one-dimensional (1D) and two-dimensional wave spectra were available at all the buoys in 30-min intervals. Here only the 1D spectrum $F(f)$ and a few integrated wave parameters are used, including the significant wave height H_s, mean wave period $T_{0,2}$, and partial wave height $H_{s,i}$ (Rogers and Wang 2007; Liu et al. 2019), defined by

$$H_s = 4\sqrt{\int_{f_{min}}^{f_{max}} F(f)\,df}, \tag{17}$$

$$T_{0,2} = \sqrt{\frac{\int_{f_{min}}^{f_{max}} F(f)\,df}{\int_{f_{min}}^{f_{max}} f^2 F(f)\,df}}, \quad \text{and} \tag{18}$$

$$H_{s,i} = 4\sqrt{\int_{f_{l,i}}^{f_{h,i}} F(f)\,df}. \tag{19}$$

A consistent maximum frequency $f_{max} \simeq 0.49$ Hz ($T \sim$ 2 s) was adopted for comparisons between observations and WW3 results. For $H_{s,i}$, the overlapping frequency range of buoys and models (i.e., [0.045, f_{max}] Hz) is divided into three bands with band boundaries locating at $f_{h,i} = 1/9, 1/5$ Hz, $i = 1, 2$ (i.e., $T \in [9, 22]$ s, $T \in [5, 9]$ s,

and $T \in [2, 5]$ s, respectively). Examination of $H_{s,i}$ provides more insights into model performance of simulating wave energy at different frequency bands.

For the WW3 simulations, we used the specific two-curvilinear-grid system described in Collins and Rogers (2017). The outer 10-km grid (G01; blue box in Fig. 1a) covers longitudes ranging from 90° to 270°E and extends southward from the North pole to the northern Bering Sea. An inner grid (G02; red box in Fig. 1a) with a higher spatial resolution ($\sim$5 km) was nested into G01 to refine the simulation surrounding the study area.

We chose the source term package ST4 (Ardhuin et al. 2010) for computing $S_{in} + S_{ds}$ terms, and the discrete interactive approximation (DIA) approach (Hasselmann et al. 1985) for estimating S_{nl}. All the other model attributes are summarized in Table 2, including the frequency and direction grids, numerical time steps, wind and ice forcing, simulation period, and so on. The related technical details can be found in Rogers et al. (2016) and Collins and Rogers (2017). A relatively low value (1.1) for β_{max}, a tuning parameter controlling the strength of S_{in} (Ardhuin et al. 2010), was adopted for this case. Collins and Rogers (2017) showed that using such value with the Navy Global Environmental Model (NAVGEM) wind forcing (Hogan et al. 2014), WW3 fits the best to measurements from the open-water buoy (AWAC in Fig. 1b). During this wave event, the ice prevalent at the sea surface, mainly consisting of pancake and frazil ice (Rogers et al. 2016), was 2–40 cm thick. Smith et al. (2018) reported a considerable ice melting occurred during this storm event. The ice concentration data provided by the Advanced Microwave Scanning Radiometer 2 (AMSR2; Kaleschke and Tian-Kunze 2016) were adopted as the forcing for our simulations (Collins and Rogers 2017, and our
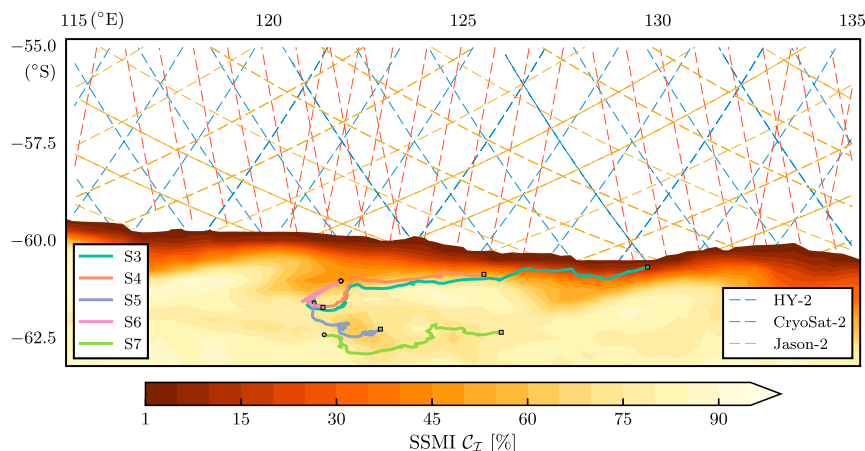
FIG. 2. Wave measurements (reference data) used in the simulation of waves in the Antarctic MIZ. Colored solid lines: tracks of five WIIOS sensors during 23 Sep–10 Oct 2012; colored dashed lines: tracks of satellite radar altimeters (blue for HY-2, red for *CryoSat-2*, and yellow for *Jason-2*) over the same period. The shaded contour illustrates the mean ice concentration C_I from 23 Sep to 10 Oct 2012.

Table 2). These satellite C_I records were found in good agreement with ship-based ice measurements (Cheng et al. 2017), showing a correlation coefficient of about 0.8 over the simulation period we concern (section S2). Meanwhile, it appears that the AMSR2 swath data (~5.3 hourly; Collins and Rogers 2017) have well resolved the spatial and temporal variation of the ice cover, particularly for the ice melting (Fig. S2). Estimating the thickness of ice h_i in the MIZ remains as one very challenging task (Huntemann et al. 2014; Ricker et al. 2017). For simplicity, we have adopted an intermediate constant ice thickness $h_i = 0.15$ m in our simulations. It should be mentioned, however, that using spatially and temporally variable h_i data from the Soil Moisture and Ocean Salinity (SMOS; Huntemann et al. 2014) does not provide better, *calibrated* model results (sections S2 and S5).

b. SIPEX II voyage 2012

During Sea Ice Physics and Ecosystem Experiment (SIPEX) II, five waves-in-ice observation systems (WIIOS; Kohout and Williams 2015) were deployed on the first-year Antarctic sea ice floes on 23–24 September 2012 to monitor spectral evolution of ocean surface waves in the MIZ. Figure 2 (colored solid lines) shows the drifting tracks of these five wave sensors from 23 September to 10 October 2012. One-dimensional wave spectra $F(f)$ at wave periods from 4.16 to 24.38 s were reported at 3-hourly intervals. In this case, we used an upper-limit frequency $f_{max} \simeq 0.24$ Hz for the comparison between simulations and observations. The frequency band boundaries defining the partial significant wave height $H_{s,i}$ were also slightly changed as $f_{h,i} = 1/16, 1/8$ Hz, $i = 1, 2$ (i.e., $T \in [16, 24]$ s, $T \in [8, 16]$

s, and $T \in [4, 8]$ s, respectively) because the averaged $T_{0,2}$ was higher in this case than in the *Sikuliaq* case (12 versus 7 s; section 5).

Unlike the previous case, we used a traditional equally spaced (0.25°) longitude–latitude grid here. The model domain is bounded within 100°–150°E of longitude and 75°–45°S of latitude, exactly following Li et al. (2015). The boundary conditions were provided by a global run with a grid resolution of 0.5° (Liu et al. 2019). Ice concentration C_I was sourced from the Special Sensor Microwave Imager (SSM/I) data (daily, 12.5 km; Kaleschke and Kern 2006). Once again, all the details about the setup of WW3 model are presented in Table 2. The ice floes on which the WIIOS wave sensors were deployed were on average 0.5–1.0 m thick (Toyota et al. 2016). Following Kohout et al. (2016), we adopted a constant ice thickness h_i of 0.75 m in our simulations. Adopting h_i from the Climate Forecast System version 2, as in Li et al. (2015, 2017), provides very similar, calibrated model results (not shown). The comparisons of open-water H_s between WW3 simulations and altimeter observations sourced from Liu et al. (2016a; colored dashed lines in Fig. 2) suggest $\beta_{max} = 1.0$ for S_{in} gives the best performance when the winds from the NCEP Climate Forecast System Version 2 (CFSv2; Saha et al. 2014) are used (see section S3).

c. Contribution from other source terms

Over the previous four decades, field experimentalists and ice modelers have customarily neglected the effect of other physical processes (i.e., S_{in}, S_{ds}, and S_{nl}; hereafter also referred to as S_{other} for brevity) on waves

in the ice-covered ocean (e.g., Wadhams et al. 1986; Williams et al. 2013a; Squire and Montiel 2016, among others). Nonetheless, Li et al. (2015) indicated that S_{in} and S_{nl} may play a considerable role in determining the *apparent* attenuation rate of ice-coupled waves, particularly for large, storm-generated waves (say, $H_s > 3$ m). It is therefore interesting to examine that under the scaling framework proposed by Masson and Leblond (1989) [(5)], how much differences S_{other} could induce in model results. For this reason, we modified (5) slightly by including an additional binary parameter Ψ so that we can flexibly switch on/off S_{other}:

$$S_T = \Psi[(1 - C_I)(S_{in} + S_{ds}) + S_{nl}] + C_I S_{ice}$$
$$= \Psi S_{other} + C_I S_{ice}, \qquad (20)$$

$$\Psi = \begin{cases} 1, & \text{for} \quad C_I = 0 \\ \psi, & \text{for} \quad C_I > 0 \end{cases}. \qquad (21)$$

A setup of $\psi = 1$ signifies the full utilization of S_{other}, whereas $\psi = 0$ denotes S_{other} is switched off in the ice-infested ocean ($C_I > 0$). It should be stressed that, as prescribed in (20), S_{other} refers to the sum of the *scaled* (reduced) S_{in} and S_{ds} terms and *unscaled* (full) S_{nl} term.

5. Results

All the three sea ice models require a priori knowledge of the corresponding rheological parameters [(G, η) for the EFS and RP models and η for the M2 model]. At this stage, however, these ice properties are largely unexplored (Mosig et al. 2015; Cheng et al. 2017). Therefore, what we really examine is the capability of these ice models to fit field measurements [e.g., H_s, $F(f)$, k_i], similar to previous works (e.g., Li et al. 2015; Rogers et al. 2016). The brute force mapping approach (Tolman 2010) was used to find the optimal rheological parameters which minimize the root-mean-square error (RMSE; ϵ) of the WW3-simulated wave height H_s (section S4). The optimization procedure utilizes the full model setup (i.e., $\psi = 1$), and the resulting optimal (G, η) for the two cases are summarized in Table 3. We found that the RP model could fit the observations in both cases with $G \simeq 0$ Pa. Consequently, the RP model (13) is well approximated by (15), particularly for $T > 5$ s (section S9). It is clear from (15) and (16) that for h_i fixed, the RP and M2 models will yield very close results given that $\eta_{RP} \simeq \eta_{M2} h_i$. This is well evidenced in Table 3 (see also Fig. 10). Therefore, unless otherwise necessary, we will show results from the M2 model only for limiting the number of plots (see sections S5 and S6 for the RP results).

Hereinafter, for each case, we have run WW3 in three different ways:

TABLE 3. Optimal rheological parameters (G, η) for the three ice models in two selected cases. The units of η for the EFS, RP and M2 models are m² s⁻¹, kg m⁻² s⁻¹ and kg m⁻³ s⁻¹, respectively. Biases (m) of the simulated H_s from the full, zero-S_{ice}, and zero-S_{other} simulations (b_f, b_{zi}, b_{zo}) are also presented together with the metric R_I indicating the relative importance of S_{other} and S_{ice} in (22).

Case	Model	G (Pa)	η	b_{zi}	b_f	b_{zo}	R_I (—)
Sikuliaq	EFS	1.0[a]	3.2×10^4	0.45	0.12	0.06	0.18
	RP	1.0[a]	2.0		0.16	0.05	0.38
	M2	—	14.0		0.16	0.05	0.38
SIPEX	EFS	4.0×10^{12}	1.6×10^7	1.46	0.06	0.04	0.01
	RP	1.0[b]	2.2		0.09	0.08	0.01
	M2	—	3.0		0.11	0.10	0.01

[a] It is reasonable to assume the elasticity of loose pancake and frazil ice present in the *Sikuliaq* case is minimal (Rogers et al. 2016). Nonetheless the solver we developed for the EFS and RP models does not allow $G = 0$ Pa. Therefore, we have simply set $G = 1$ Pa here.

[b] It is expected that elasticity should play a role in the SIPEX case due to the large floe size (Meylan et al. 2014). For $G < 10^6$ Pa, however, the elasticity only affects the RP-estimated k_i at low wave periods ($T < 5$ s; Fig. S15), and we found the ϵ_{H_s} minimized at G $\simeq 0$ Pa.

1) the *full* simulation with $\psi = 1$ and nonzero h_i specified in Table 2 (i.e., S_{other} is always active and S_{ice} is estimated according to different ice models);

2) the *zero-S_{ice}* simulation with $\psi = 1$ and $h_i = 0$ m (i.e., S_{ice} is switched off in this specific simulation); and

3) the *zero-S_{other}* simulation with $\psi = 0$ but nonzero h_i [i.e., S_{other} is deactivated in the ice-infested ocean only ($C_I > 0$)].

The comparison between the full and zero-S_{ice} simulations was designed to check the importance of S_{ice} in damping wave energy, and the comparison between the full and zero-S_{other} simulations will allow us to examine the sensitivity of the simulated H_s to S_{other}. It may be worth mentioning that when the sea is fully covered by ice ($C_I = 100\%$), S_{other} essentially becomes S_{nl} only in (20), and thus the difference between simulations 1 and 3 will provide insight into the importance of S_{nl} in this model.

a. *R/V* Sikuliaq *cruise 2015*

Figure 3 shows the comparison of H_s and $T_{0,2}$ between the model results and buoy measurements for the *Sikuliaq* case. The corresponding comparison of the partial wave height $H_{s,i}$ is illustrated in Fig. 4. A total of 497 model–buoy collocations are obtained, and error statistics presented include bias b, RMSE ϵ, correlation coefficient ρ, and scatter index SI (section S3).

The zero-S_{ice} or nondissipative simulation (Fig. 3a) clearly overestimates H_s with an overall bias of 0.45 m and RMSE of 0.53 m. By introducing the ice-induced damping, the full
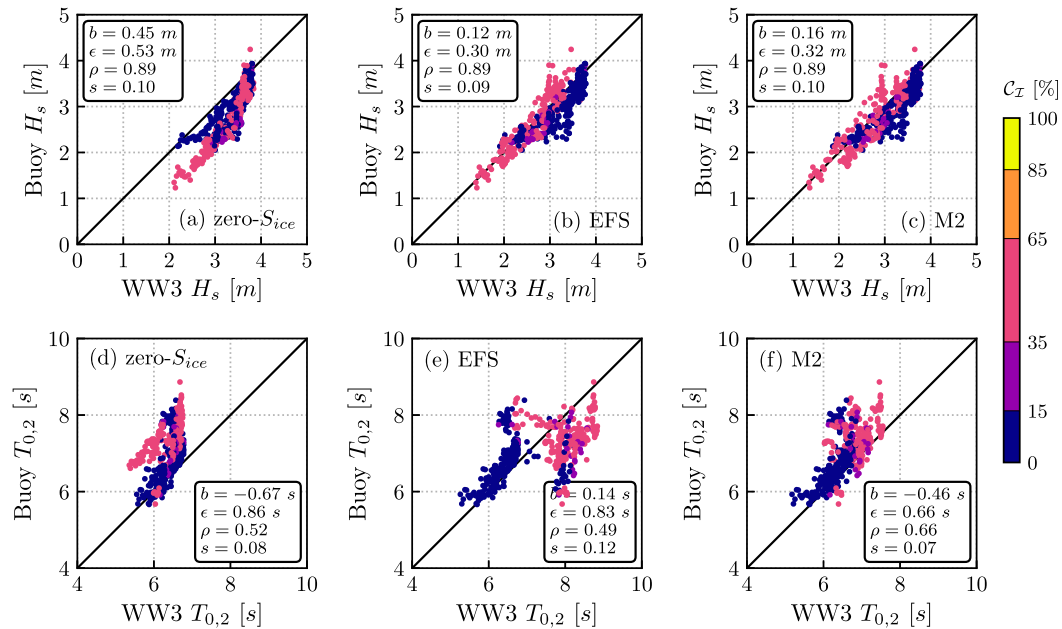
FIG. 3. Comparison of (top) significant wave height H_s and (bottom) mean wave period T_{02} between R/V *Sikuliaq* cruise-collected buoy measurements and model results according to (a),(d) zero-S_{ice} ($h_i = 0$ m), (b),(e) full EFS, and (c),(f) full M2 simulations. The color of the model–buoy collocations indicates the AMSR2 ice concentration C_I.

simulations with the EFS and M2 models (Figs. 3b,c) yield similarly improved performance in specifying H_s: lower bias (~0.15 m) and reduced ϵ (~0.3 m) but almost unchanged ρ (~0.89) and scatter index (0.10).

The effect of S_{ice} is more noticeable in the comparison of wave period $T_{0,2}$. The zero-S_{ice} simulation (Fig. 3d) remarkably underestimates $T_{0,2}$ by 0.7 s with a moderate ρ of 0.5. The full EFS simulation (Fig. 3e) shows a clearly improved b (0.1 s) but a marginally worse (0.8 s). The other two metrics (ρ and SI) become worse due to the considerable overestimation of periods greater than 7 s. The full M2 simulation (Fig. 3f) presents the best performance, as represented by the lowest ϵ, SI, and highest ρ. Overall, $T_{0,2}$ is still underestimated by 0.6 s.

Inspection of Fig. 4 suggests that the most striking effect of S_{ice} in reducing wave energy appears at the high-frequency band ($H_{s,3}$ for $T < 5$ s; Figs. 4c,f,i), as expected. The zero-S_{ice} simulation apparently overestimates $H_{s,3}$ even for very low C_I cases (blue points in Fig. 4c), indicating some small-scale ice features (e.g., ice melt and drift; Smith et al. 2018; Alberello et al. 2020), which could affect the attenuation of waves dramatically (Sutherland et al. 2018), was unresolved by the AMSR2 C_I data and our constant h_i assumption. For moderate C_I (pink points), the full M2 model is in good agreement with observations (Fig. 4i), whereas the full EFS simulation underestimates $H_{s,3}$ considerably, suggesting its k_i might be too high at $T < 5$ s and explaining the clear

overestimation of $T_{0,2}$ (Fig. 3e). The EFS and M2 models perform similarly at the intermediate frequency band ($T \in [5, 9]$ s; Figs. 4e,h) and sea ice plays a limited role at the low frequency band ($T > 9$ s; Figs. 4a,d,g).

The deactivation of S_{other} in ice-covered seas (i.e., $\psi = 0$) makes some differences in the modeled H_s and $T_{0,2}$ between the zero-S_{other} and full simulations. In general, H_s ($T_{0,2}$) from the zero-S_{other} simulations is around 0.1 m lower (0.1 s higher) than that from full simulations (Table 3; section S5).

b. SIPEX II voyage 2012

The comparisons of H_s, $T_{0,2}$, and $H_{s,i}$ between model results and buoy observations for the SIPEX case are shown in Figs. 5 and 6, respectively. In this case, H_s is significantly overpredicted by the zero-S_{ice} simulation (Fig. 5a; $b = 1.5$ m, $\epsilon = 1.7$ m). The model performance is remarkably enhanced by the full simulations (Figs. 5b,c) due to the inclusion of the S_{ice} term. Each of the full EFS and M2 simulations shows a considerably reduced bias ($b \leq 0.1$ m), and an ϵ around 0.6 m. The improvements in other error metrics (ρ and SI) are also fairly marked. Similar results can be found in the comparisons of $T_{0,2}$. The zero-S_{ice} simulation (Fig. 5d) yields a $T_{0,2}$ poorly correlated with observations ($\rho = 0.18$), and the full simulations (Figs. 5e,f) augment the correlation considerably (0.5–0.6). Nonetheless, $T_{0,2}$ is still noticeably underestimated by about 2 s. Figure 6 demonstrates that the effect of S_{ice} is clearly visible at both intermediate and high-frequency bands ($T < 16$ s),
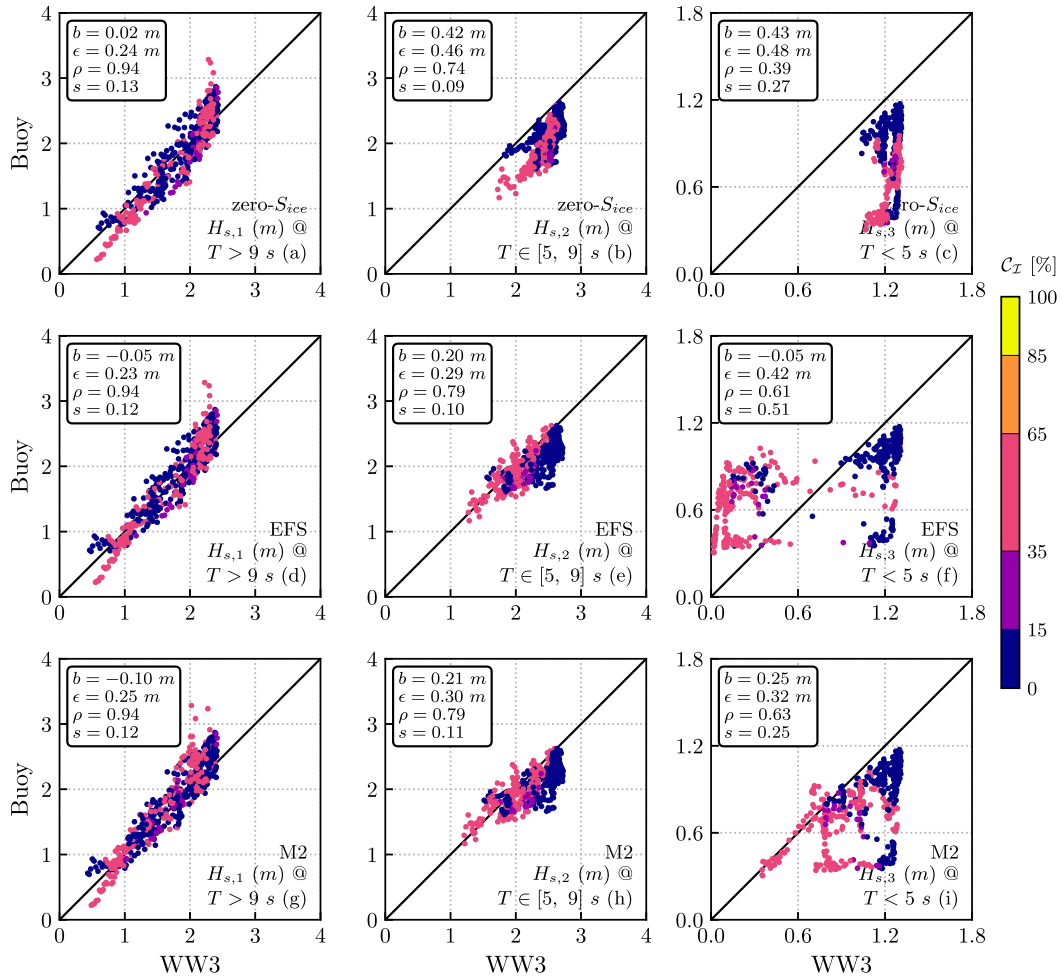
FIG. 4. Comparison of partial wave height (left) $H_{s,1}$ for $T > 9$ s, (center) $H_{s,2}$ for $T \in [5, 9]$ s, and (right) $H_{s,2}$ for $T < 5$ s between buoy observations and model simulations according to (a)–(c) zero-S_{ice} ($h_i = 0$ m), (d)–(f) full EFS, and (g)–(i) full M2 simulations. The axis limits are different for the right column.

and the full M2 simulation performs the best at these two frequency bands.

Unlike the previous case, the zero-S_{other} simulations here only differ marginally from the full simulations. Significant wave height H_s from the former is only up to 0.02 m lower than that from the latter (Table 3; section S6).

6. Discussions

a. Impact of other source terms S_{other}

The previous section suggests that the contribution from other source terms S_{other} is quantitatively different between the two cases. The relative importance of S_{other} and S_{ice} may be *roughly* quantified by

$$R_I = \left| \frac{b_f - b_{\text{zo}}}{b_f - b_{\text{zi}}} \right|, \tag{22}$$

where b_f, b_{zi}, and b_{zo} are the biases of modeled H_s from the full, zero-S_{ice}, and zero-S_{other} simulations, respectively. Note that R_I can only imply the relative precedence of S_{other} and S_{ice} in determining wave height H_s. It provides little information about the impact of these terms in specifying the high-frequency tail of the wave spectrum since wave energy at this frequency range is very limited.

For the *Sikuliaq* case, R_I based on the simulations with the EFS and M2 models are 0.18 and 0.38 (Table 3), respectively. By contrast, the impact of S_{other} in the SIPEX case is considerably lower ($R_I = 0.01$; Table 3), indicating that S_{other} can be ignored in this specific case. These conjectures are further corroborated in Fig. 7, where different source terms are quantified for four wave spectra from the WW3-M2 full simulations, including two spectra from each case study. Two spectra correspond to relatively mild sea states (Figs. 7a,c; $H_s = 1.8, 1.1$ m) and the other two are moderately energetic
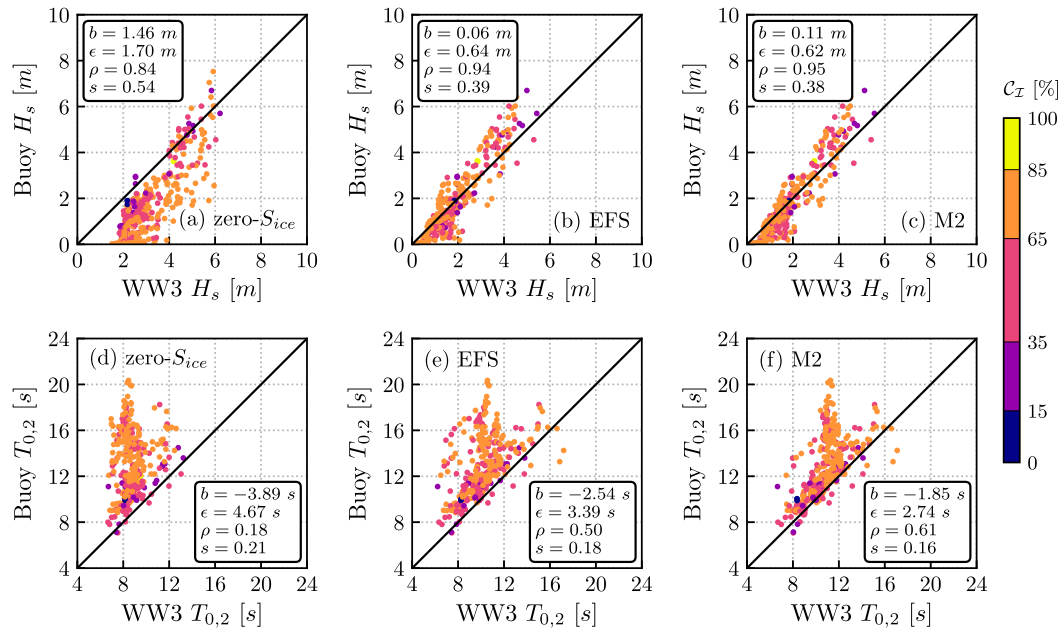
FIG. 5. As in Fig. 3, but for the SIPEX case (400 collocations are obtained). The color of the model–buoy collocations indicates the SSM/I ice concentration C_I.

(Figs. 7b,d; H_s = 3.3, 4.8 m). For comparison purpose, the so-called growth rate $\beta(f) = S(f)/F(f)$ (in s^{-1}) (e.g., Donelan et al. 2006) is shown in these plots. All the source terms have been scaled with ice concentration C_I properly as in (5). Note that a maximum frequency of 0.25 Hz is chosen here as limited by the highest sampling frequency of the WIIOS sensors (section 4b). Results from the EFS and RP models present the qualitatively similar features, and therefore are not reproduced here (section S7).

For the two *Sikuliaq* spectra (Figs. 7a,b), the sea state is dominated by wind sea, as the wave ages $\delta = c_p/U_{10}$ are about 0.98, where c_p is the peak phase velocity and U_{10} is the hindcast wind speed at 10 m above sea level.[1] Inspection of these two panels suggests (i) the wave breaking term S_{ds} plays a negligible role, (ii) S_{in} and S_{nl} are comparable to S_{ice} for frequencies higher than f_p, and (iii) for long waves ($f < f_p$), S_{in} and S_{nl} can be noticeably higher than S_{ice}, particularly for energetic waves (Fig. 7b). These results demonstrate the significant contribution from S_{other} or more specifically from S_{in} and S_{nl} terms. Comparisons of wave spectra from the full simulation (F_1^m; coral solid line in the insets) and from the zero-S_{other} simulation (F_0^m; blue dashed line in the insets) illustrate the main consequence of S_{other} is the slightly higher spectral peaks and higher wave heights.

In addition, it gives rise to a marginal, but still appreciable, downshifting of the spectral energy.

For the two SIPEX spectra (Figs. 7c,d), the sea state is dominated by old swell as wave age $\delta > 1.48$, and S_{other} is considerably lower than S_{ice}. Accordingly, it is reasonable to conclude that S_{ice} dominates S_{other} in both calm and energetic seas in this case. Similar to Figs. 7a and 7b, β_{in} and β_{nl} are slightly higher in the energetic case than in the mild case. Clearly, the growth rate β arising from S_{other} is significantly lower in the SIPEX case than in the *Sikuliaq* case, which is primarily because sea states in the latter case are relatively young. Young and van Vledder (1993, their Fig. 3) clearly demonstrated that the magnitude of S_{in} and S_{nl} reduce as waves grow. It should be further noted that the ice conditions in these two cases are completely different. The SIPEX case represents remarkably higher ice concentration C_I (Fig. 5 versus Fig. 3) and larger ice floes (Meylan et al. 2014; Rogers et al. 2016). Meanwhile, observations collected by the SIPEX cruise were much deeper into the ice field (Fig. 2 versus Fig. 1). All these factors could possibly contribute to the insignificant role of S_{other} in this specific case.

The interplay of the ice-decay term S_{ice} and wave breaking term S_{ds} deserves some attention. The state-of-the-art parameterizations of wave breaking incorporate a threshold mechanism, that is, ocean waves will not break unless the wave spectrum $F(f)$ exceeds a threshold spectral value $F_T(f)$ (Babanin et al. 2010). The ice-induced wave damping keeps $F_T(f)$ mostly below $F_T(f)$, and thus

---

[1] Donelan et al. (1985) suggested wave spectrum with δ lower (greater) than 1.2 would be considered as wind-sea (swell).
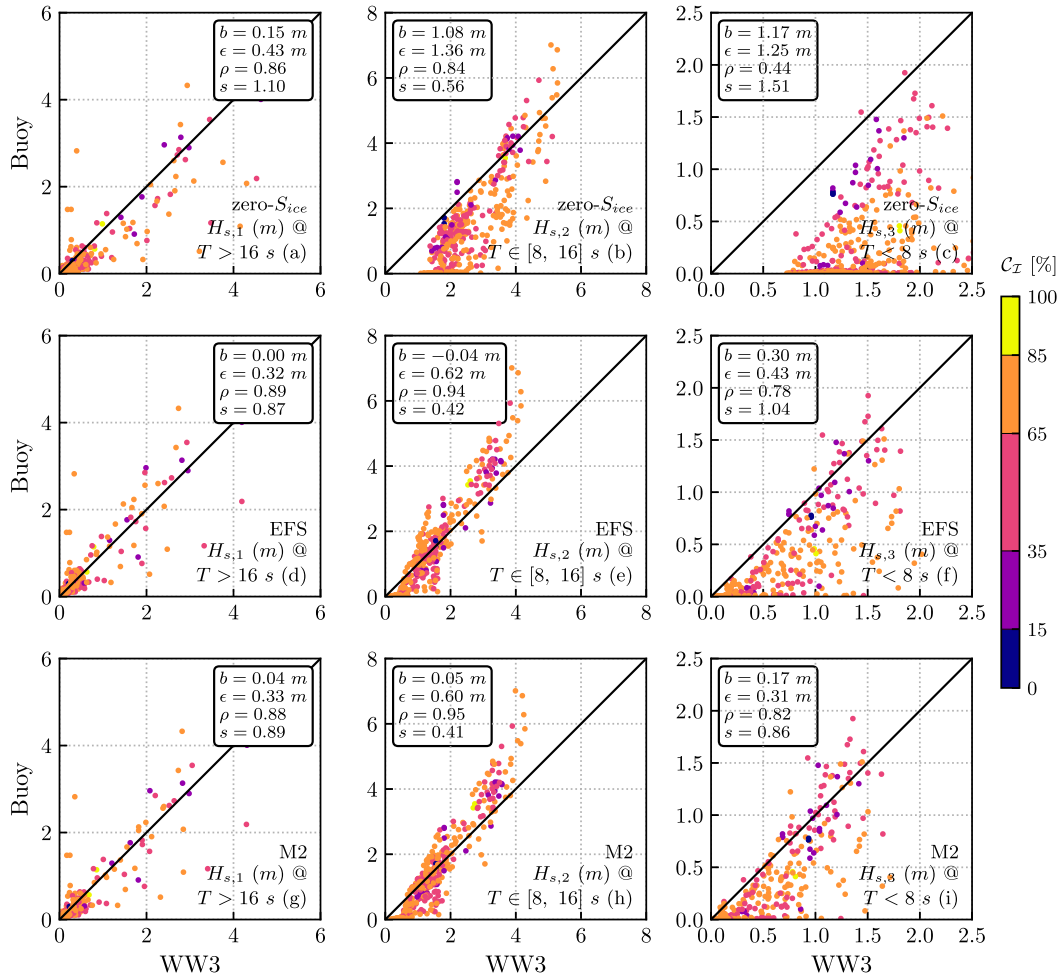
FIG. 6. Comparison of partial wave height (left) $H_{s,1}$ for $T > 16$ s, (center) $H_{s,2}$ for $T \in [8, 16]$ s, and (right) $H_{s,3}$ for $T < 8$ s between buoy observations and model simulations according to (a)–(c) zero-S_{ice} ($h_i = 0$ m), (d)–(f) full EFS, and (g)–(i) full M2 simulations. The axis limits are different for the right column.

effectively shuts down S_{ds}. The validity of these threshold-based S_{ds} parameterizations in ice-covered oceans, however, should be further investigated in the future.

b. Wave height decay in the SIPEX case

Based on the same measurements collected in the SIPEX case, Kohout et al. (2014) found the wave height decay (dH_s/dx) to be exponential for small waves ($H_s < 3$ m) and to be almost linear for strong waves ($H_s > 3$ m) (see the gray line in Fig. 8). The authors suggested that such behavior may be attributed to the downshifting of spectral energy due to the nonlinear four-wave interactions (S_{nl}). Later, a numerical study of the same case by Li et al. (2015) also indicated that S_{nl} can be more effective in the stormy sea states ($H_s > 3$ m) than in the calm seas ($H_s < 3$ m) and thus "contribute significantly to the less 'apparent' attenuation" of large waves. These qualitative arguments are not supported

by our quantitative findings here since S_{nl} is far less than S_{ice} in this case (Figs. 7c,d) and hence hardly contributes to the linear decay behavior of large waves. It is thus interesting to examine whether our results from the zero-S_{other} simulations can reproduce the transition behavior from the exponential decay regime to the linear decay regime.

Figure 8 presents the box-and-whisker plot of the attenuation rates of wave height dH_s/dx (blue box with black whisker) as a function of H_s, as estimated from the WIIOS buoy measurements (Fig. 8a) and our zero-S_{other} simulations with different ice models (Figs. 8b,c).[2] It is evident that the two zero-S_{other} simulations reproduce the flattening of dH_s/dx for H_s beyond 3 m (see the purple lines in Fig. 8) reasonably well. This manifests

---

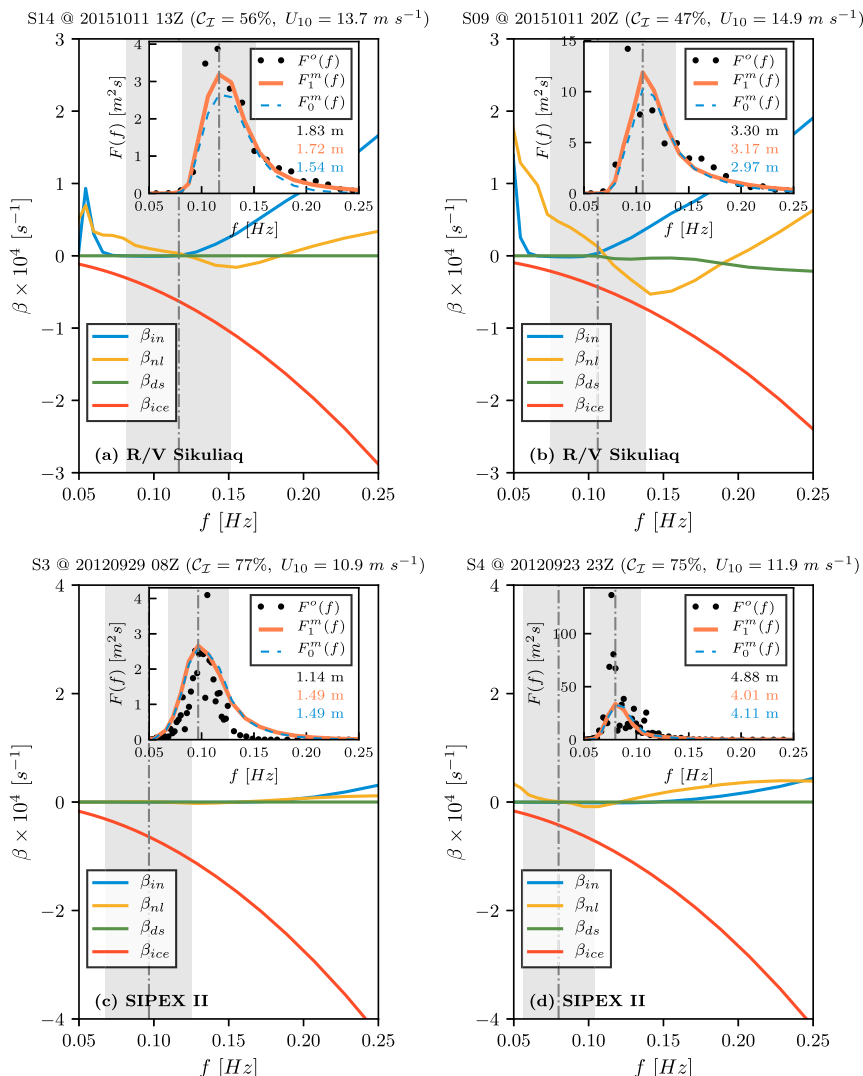[2] The results for the full simulations are shown in section S8.

FIG. 7. Growth rate β (blue: β_{in}, yellow: β_{nl}, green: β_{ds}, and red: β_{ice}) vs wave frequency f at buoys (a),(b) S14 and S09 from the R/V *Sikuliaq* case and (c),(d) S3 and S4 from the SIPEX case, as estimated by the full M2 simulations. The corresponding time, ice concentration C_I, and wind speed U_{10} are printed in the title of each panel. The insets display the comparison of the measured [black dots (•): $F^o(f)$] and simulated one-dimensional wave spectra [coral solid line: $F_1^m(f)$ from the full simulation; blue dashed line: $F_0^m(f)$ from the zero-S_{other} simulation], as well as the corresponding wave heights (different colored text in the inset: black: H_s^o; coral: $H_{s,1}^m$; blue: $H_{s,0}^m$). The vertical dash–dotted line (gray-shaded area) highlights the peak frequency f_p (dominant wave spectral band $f_p \pm 0.3 f_p$) of $F_1^m(f)$.

that the trend of dH_s/dx discovered by Kohout et al. (2014) can be well explained by the attenuation models we selected *without the utilization of S_{nl}* in the ice-infested seas. To further explain the linear decay of large waves, we show the corresponding box-and-whisker plot of the peak frequency f_p (red box with black whisker) as well. Note that the measured wave spectra $F(f)$ with small wave heights are fairly noisy, and consequently the f_p values for the first H_s bin ($0 < H_s < 1$ m) shown in Fig. 8a are not

necessarily reliable. By excluding that spurious bin, we can find a clear downward trend in the measured f_p as H_s increases. Such decline of f_p is also marked in our zero-S_{ice} simulations (Figs. 8b,c). A well-established feature of the open-water, fetch-limited wind seas is that H_s and f_p correlate strongly due to the dominant role of S_{nl} in the evolution of wave spectrum (Hasselmann et al. 1973). The larger waves corresponding to lower peak frequencies as shown in Fig. 8 are likely caused by i) the S_{nl} term active in
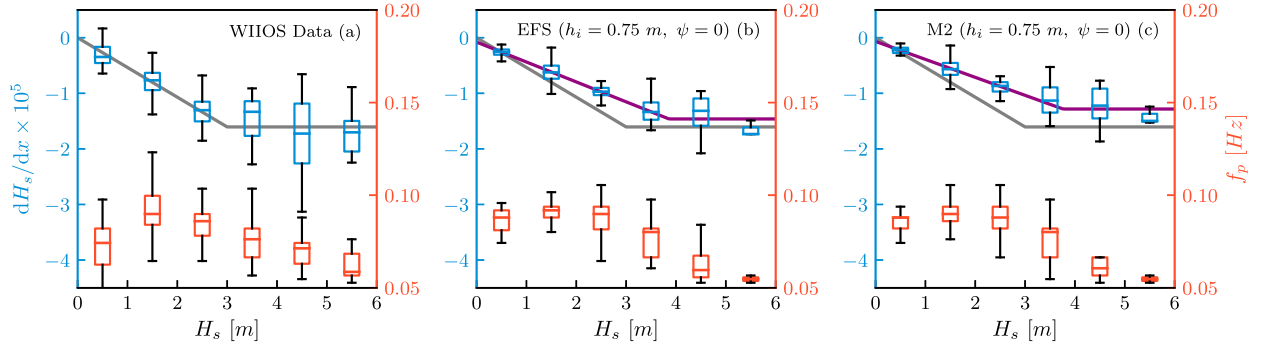
FIG. 8. Box-and-whisker plots of (left y axis) attenuation rates of wave height dH_s/dx (blue box with black whiskers) and (right y axis) peak wave frequency f_p (red box with black whiskers) as a function of H_s according to (a) WIIOS buoy measurements and the zero-S_{other} simulations (i.e., $h_i = 0.75$ m and $\psi = 0$) with the (b) EFS and (c) M2 models. The gray line shows the empirical form of dH_s/dx derived from WIIOS data by Kohout et al. (2014). The purple line is fitted from the median values of model results.

the *open water* before waves enter the ice fields and ii) the low-pass filtering effect of sea ice (e.g., Sutherland and Gascard 2016). As f_p decreases, the dominant wave components of a wave spectrum (say, $f_p \pm 0.3 f_p$; Babanin et al. 2001) will experience reduced damping by ice, and finally result in the flattening of dH_s/dx for $H_s > 3$ m in this case.

Although insignificantly affecting overall wave energy (H_s) in the SIPEX case, S_{other} does change the spectral distribution of the apparent attenuation rate [i.e., $\alpha_a(T)$]. Figure 9 presents the α_a estimated from the WW3-modeled $F(f)$ at the WIIOS locations according to the full and zero-S_{other} simulations, respectively. Following Meylan et al. (2014), the apparent attenuation α_a is defined as

$$\alpha_a(T) = \frac{|\ln(F_i^m/F_j^m)|}{\Delta x_{i,j}}, \qquad (23)$$

where $F_i^m(T)$ and $F_j^m(T)$ are modeled wave spectra at two adjacent WIIOS sensors, $\Delta x_{i,j}$ is the spatial distance, and waves are assumed to travel directly south to higher latitudes (Fig. 2). Clearly, when S_{other} is introduced, the estimated α_a at low periods ($T \leq 5$ s) is noticeably reduced, particularly for the WW3-EFS simulations (Fig. 9a). The α_a computed from modeled spectra using (23) appreciably deviates from the prescribed value by different sea ice models at $T > 15$ s, implying the southward-propagating assumption does not hold well for these frequency ranges. Meanwhile, it suggests caution should be exercised when one applies a power-law fitting to sufficiently low, field measured α_a due to the uncertainty involved (see also Rabault et al. 2019).

c. Wavenumber k_r and attenuation rate k_i

An analysis of the wavenumber k_r and attenuation rate k_i in shown in Fig. 10 where a direct intercomparison of

these properties from different sea ice models (using the rheological parameters specified in Table 3), as well as field observations when available, is presented.

For the *Sikuliaq* case, the measurements from Collins et al. (2018, WB3 only) suggest the deviation of k_r from the open-water value k_0 is not significant unless the wave period becomes small enough (gray box-and-whisker plots in Fig. 10a). For $T \leq 3$ s, the measured wavelength is slightly reduced when compared against open-water values ($k_r/k_0 > 1$). Among the three ice models, only the RP model yields a qualitatively similar behavior. The M2 model assumes no change in wavelength, and the EFS model presents a lengthened λ for $T < 4$ s. The RP/M2-estimated k_i is slightly lower than field observations from Cheng et al. (2017, WE3 only; in terms of median values), but still falls in the measured range (Fig. 10b) and compares well with the model inversion results of Rogers et al. (2018a, WA3-SWIFT therein) (Fig. 10c). Consistent with field observations and as prescribed by (15) and (16), the RP/M2 model follows a power law of $k_i \propto \omega^3$. By contrast, the EFS model shows two different power laws: $k_i \propto \omega^{11}$ for $T > 4$ s as suggested by (14) and $k_i \propto \omega^{3/2}$ for $T < 3$ s (Fig. 10c), resulting in significant overestimation (underestimation) of k_i at low (high) periods. This also explains its overprediction of $T_{0,2}$ and underspecification of $H_{s,3}$ at moderate C_I (Figs. 3e and 4f).

Only k_i observations were available for the SIPEX case (Figs. 10e,f), which roughly conformed to $k_i \propto \omega^2$ (Meylan et al. 2014, 2018). The RP/M2-estimated k_i is in good agreement with, but slightly lower than, the data (Fig. 10f). The EFS model is closer to observations for $T \in [10, 20]$ s ($k_i \propto \omega^{3/2}$), but again transforms into a power law ($k_i \propto \omega^{11}$) at higher periods. Overall, the estimated k_i values from all the three models are well within the observed range (Fig. 10e).
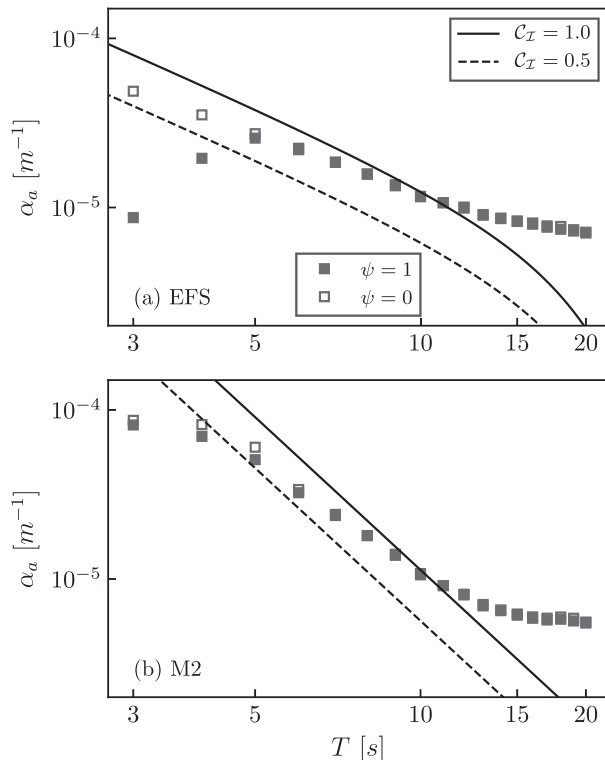
FIG. 9. Apparent attenuation rates α_a calculated from the WW3-simulated wave spectra at buoy locations (solid square: full simulation with $\psi = 1$, empty square: zero-S_{other} simulation with $\psi = 0$) for the SIPEX case. Only spectra values $F(f)$ greater than 10^{-3} m^2 s were considered. For clarity, we show the median values only of different wave period bins. (a) WW3-EFS and (b) WW3-M2. The solid (dashed) line presents α_a directly estimated by the corresponding sea ice model (i.e., $\alpha_a = 2C_I k_i$ using rheological parameters in Table 3) for $C_I = 100\%$ ($C_I = 50\%$).

It should be highlighted that results shown in Fig. 10 are derived with the specific values of (G, η). Distinct behaviors of k_r and k_i could be obtained when these rheological parameters change, particularly for the two VE models [see Fig. A1, section S9, and Mosig et al. (2015)].

d. Limitations and operational forecast

The three sea ice models we select are intuitively appealing as a MIZ composed of numerous ice floes, pancake ice, and frazil present at different sizes (e.g., Alberello et al. 2019) is mapped onto a modified dispersion relation with one/two rheological parameters only. These models, particularly the two VE ones, however, are practically difficult in the sense that estimating *effective* G and η for different ice covers requires tremendous efforts since these parameters could vary over several orders of magnitude (section S4; see also Cheng et al. 2017). Furthermore, none of these effective rheological parameters is directly related to the physical properties of ice floes/sheets measured in the laboratory.

It is also noteworthy that the EFS-favored rheological parameters sometimes might be too unphysically large (Squire 2020). For the SIPEX case, the EFS model requires a G of $\mathcal{O}(10^{12})$ Pa (three orders of magnitude larger than the typical value for a solid ice cover) and η of $\mathcal{O}(10^7)$ m^2 s^{-1} [four orders of magnitude higher than values summarized by Cheng et al. (2017), i.e., $\eta \in [10^{-4}, 10^3]$ m^2 s^{-1}; see also Mosig et al. (2015)].

Optimizing the M2 model under different ice conditions appears less complex (i.e., only η is unknown) but remains a significant problem. More data are needed to design a reliable prototype for estimating these parameters of an effective sea ice medium. It should be mentioned that the limitation of the three ice models—that no guidance is available for setting dissipative parameters—are to some extent shared by many other dissipative theories (e.g., Liu et al. 1991; Kohout et al. 2011; see the last column of Table 1).

Despite these difficulties, it would be still beneficial for operational forecasts and wave/ice-related climate studies to take into account the ice-induced wave decay. While a more sophisticated, versatile attenuation theory awaits future research, we may simply use the M2 model with a predetermined η (e.g., $\eta \sim 10$ kg m^{-3} s^{-1}) for possible large-scale applications *at this stage*. Although the accuracy of the simulated H_s is not guaranteed, this empirical approach is certainly more advantageous than the partial-blocking approach used in most of contemporary operational wave models [e.g., Tolman (2003); IC0 in WW3DG (2019); see section S10). Other applications with fixed empirical k_i profiles (or fixed dissipative parameters) can be found in Bennetts et al. (2017), Williams et al. (2017), and Rogers et al. (2018a).

7. Concluding remarks

In the present paper, we first implemented three dissipative ice models (Mosig et al. 2015; Meylan et al. 2018) into the spectral wave model WW3 and then investigated their capability to fit field wave measurements through two case studies. The observed ice-induced wave attenuation rates k_i in these cases support a power law of $k_i \propto \omega^n$ with n between 2 and 4 (Meylan et al. 2018). The M2 and RP [especially its approximation (15)] models follow $k_i \propto \omega^3$, and as a result yield good agreement with observations. The EFS model demonstrates two different power laws: $k_i \propto \omega^{11}$ for low G and high T and $k_i \propto \omega^{3/2}$ otherwise. For the *Sikuliaq* case where $G \simeq 0$ Pa was adopted, the order 11 power law behavior caused the EFS model significantly overestimate k_i at high frequencies and accordingly clearly overpredict $T_{0,2}$ (Fig. 3e). Given these results and our previous discussions (section 6d), we may
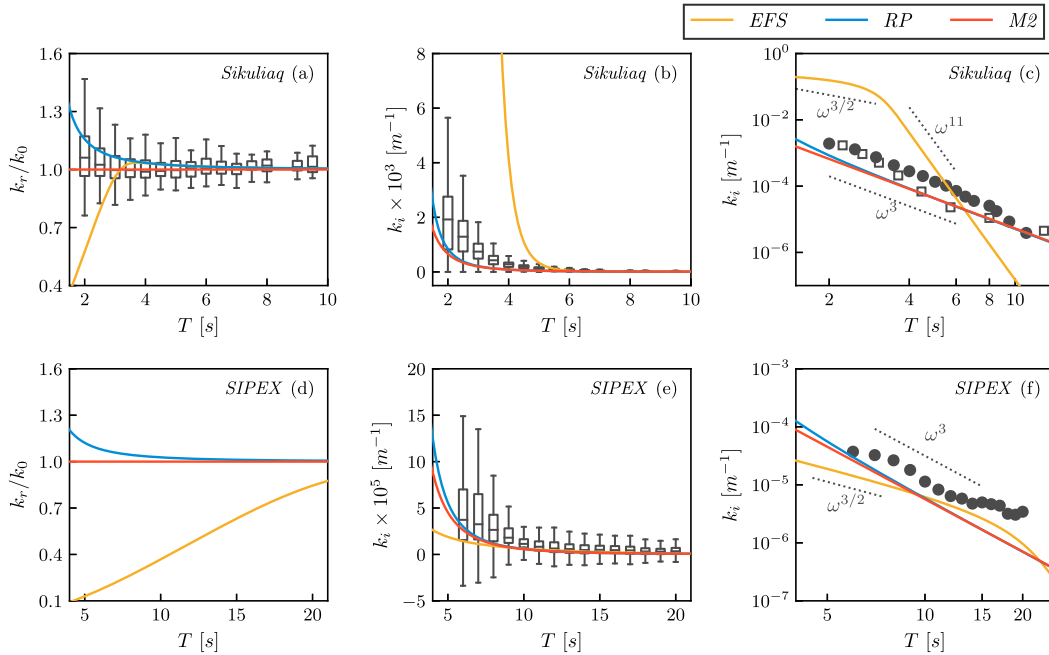
FIG. 10. Wavenumber k_r and attenuation rate k_i of ice-coupled waves as a function of wave period T for the (top) *Sikuliaq* and (bottom) SIPEX cases: (a),(d) k_r normalized by the open-water wavenumber k_0; (b),(e) k_i vs T on a linear scale; (c),(f) k_i vs T on a logarithmic scale. Box-and-whisker plots in (a), (b), and (e) present the observations from Collins et al. (2018, WB3 only), Cheng et al. (2017, WE3 only), and Meylan et al. (2014, $k_i = \alpha_a/2$), respectively. The median values of k_i observations shown in (b) and (e) are replotted as black filled circles (●) in (c) and (f), and the empty squares (□) in (c) present the inversion results from Rogers et al. (2018a,b, WA3-SWIFT therein). Slopes proportional to $\omega^{3/2}$, ω^3, and ω^{11} are also shown as references. Where applicable, k_r and k_i estimated by the EFS, RP, and M2 models (using G and η specified in Table 3) are shown in (a)–(f) as yellow, blue, and red sold lines, respectively. Note that the horizontal axis limits for the top and bottom panels are different.

conclude that the EFS is not a suitable model for simulating ice-coupled waves in the MIZ.

Operational applications of the selected ice models require a priori knowledge of the rheological parameters (G and η), which is however not available yet. We therefore suggest that the M2 model (which will become the default option for the IC5 module) with a predefined η, or alternatively other empirical k_i profiles (e.g., Rogers et al. 2018a), might be adopted for operational applications at this stage as an interim solution for lack of more "satisfactory, physically-defensible [dissipative] models at present" (Squire 2020).

Another important aspect of our paper is the sensitivity study of the precedence of S_{ice} and other source terms S_{other} [Eq. (20)] in ice-infested seas. For the SIPEX case, S_{other} is remarkably less than S_{ice} and thus plays a very limited role in determining the simulated wave energy. It is also shown that the wave height decay (dH_s/dx) reported in Kohout et al. (2014)—being exponential for $H_s < 3$ m and approximately linear for larger H_s—can be well explained by the linear attenuation theories we selected (Fig. 8). The low apparent

attenuation rate of H_s for $H_s > 3$ m therein resulted from the corresponding decreased peak frequency. However, S_{other} should not be neglected for a more general modeling purpose as we show S_{in} and S_{nl} can be comparable or even higher than S_{ice} in the *Sikuliaq* case where wave and ice conditions were very different (e.g., wind sea, low C_I, pancake ice). Furthermore, S_{other}, in particular S_{nl}, changes dramatically with spectral shape (Young and van Vledder 1993; see also Fig. 7 and section S7). Our findings here should not be taken as an indication that S_{other} can be ignored in the Antarctic MIZ but not in the Arctic MIZ.

It should be further emphasized that the precedence of S_{ice} and S_{other} is quantified here by assuming the scaling of open-water source terms in (5) suggested by Masson and Leblond (1989) is rational. To date, the validity of such scaling mechanism remains unverified, and how to compute S_{other} in ice-covered waters (e.g., S_{in} and S_{nl}), is still an unresolved problem (Rogers et al. 2016, their section 5 and references therein). Sutherland et al. (2018) reported that wave growth rates in ice-forming conditions (very sparse ice cover with some pancake/frazil ice) were slightly higher than previous
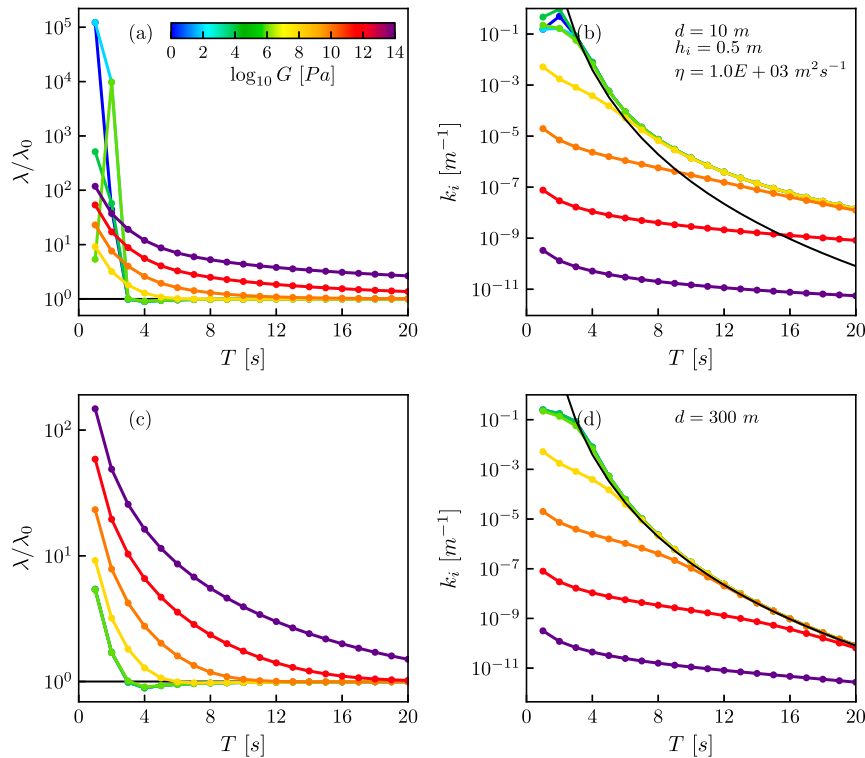
FIG. A1. (a) Normalized wavelengths λ/λ_0 and (b) attenuation rates of wave ampli-tude k_i vs wave period T, as estimated by the EFS model with the Newton–Raphson iterative solver. The solid black line in the left (right) panels highlights $\lambda/\lambda_0 = 1$ [the low-attenuation approximation (14)]. Other parameters used are $d = 10$ m, $h_i = 0.5$ m, $\eta = 10^3$ m^2 s^{-1}, and G ranging from 1 to 10^{14} Pa. (c), (d) As in (a) and (b) but for $d = 300$ m.

open-water measurements (e.g., Kahma and Calkoen 1992), indicating S_{other} may behave differently in the ice-free and ice-infested seas. More field experiments and more physically based theories of wave-ice interactions should be developed in the future.

are thankful for all comments and criticism raised by re-viewers that have improved our manuscript a lot.

APPENDIX

Solutions of the Dispersion Relations of the EFS and RP Models

For zero viscosity ($\eta = 0$ m^2 s^{-1} or 0 kg m^{-2} s^{-1}), the dispersion relations of the EFS and RP models (11)–(13) degrade to the standard thin elastic beam dispersion

$$\Re(Q)g\kappa \tanh(\kappa d) - \omega^2 = 0, \qquad (A1)$$

where $\Re(Q)$ is the real part of Q. By considering forward-going and decaying wave modes only (i.e., modes in the first quadrant of the complex k-plane with $k_r \geq 0$ and $k_i \geq 0$), the above dispersion relation has a real root, a complex root and infinitely many imagi-nary roots (Fox and Squire 1990, their Fig. 3). When $\eta \neq 0$, the roots of (A1) are perturbed slightly in the com-plex k plane and all of them become complex numbers

(Mosig et al. 2015, their Fig. 2). Specifically, the perturbed real root is the so-called dominant solution which has the most geophysical relevance (Mosig et al. 2015). Thus, the Newton–Raphson method can be utilized to solve (11)–(13) iteratively, by using the real root of (A1) as the first guess. In essence, the dispersion relations of the EFS and RP models can be transformed as follows:

$$(\mathscr{C}_1 \kappa^4 + \mathscr{C}_2)\kappa \tanh(\kappa d) - 1 = 0, \qquad (A2)$$

where $\mathscr{C}_1 = G_\eta h_i^3(1 + \nu)/6\rho_w \omega^2$, $\mathscr{C}_2 = -\rho_i h_i/\rho_w + g/\omega^2$ for the EFS model, and $\mathscr{C}_1 = G h_i^3(1 + \nu)/6\rho_w \omega^2$, $\mathscr{C}_2 = -\rho_i h_i/\rho_w + g/\omega^2 - i\eta/\rho_w \omega$ for the RP model, respectively.

For the EFS model, the numerical solver, however, may fail for small wave periods in some rare cases (particularly for shallow water depth d and low G). Figure A1 shows the EFS wavelength λ (normalized by the open-water wavelength λ_0) and attenuation rate k_i estimated by the Newton–Raphson iterative solver. The shear modulus G ranges from 1 to 10^{14} Pa and other parameters are fixed at $d = 10$ m, $h_i = 0.5$ m, $\eta = 10^3$ m^2 s^{-1}. For wave periods less than 3 s and $G \leq 10^6$ Pa, the solver shows erratic behaviors as the quasi-evanescent modes (i.e., the perturbed imaginary roots) rather than the dominant wave modes are returned. In such cases, the estimated wavelengths are unrealistically high. When the EFS model was implemented in WW3, such erratic roots were filtered by setting a minimum-allowed water depth d_{min}. By default, $d_{min} = 300$ m (Figs. A1c,d), which basically limits (11) to deepwater cases. Besides, we can also use a limiter on wave periods T_{min} (e.g., $T_{min} = 5$ s) to avoid such errors. Similar capping of attenuation rates can also be found in Doble and Bidlot (2013), where k_i (or α_s) was capped at $T = 6$ s.

REFERENCES

Alberello, A., M. Onorato, L. Bennetts, M. Vichi, C. Eayrs, K. MacHutchon, and A. Toffoli, 2019: Pancake ice floe size distribution during the winter expansion of the antarctic marginal ice zone. *Cryosphere*, **13**, 41–48, https://doi.org/10.5194/tc-13-41-2019.

——, L. Bennetts, P. Heil, C. Eayrs, M. Vichi, K. MacHutchon, M. Onorato, and A. Toffoli, 2020: Drift of pancake ice floes in the winter Antarctic marginal ice zone during polar cyclones. *J. Geophys. Res. Oceans*, **125**, e2019JC015418, https://doi.org/10.1029/2019JC015418.

Ardhuin, F., and Coauthors, 2010: Semi-empirical dissipation source functions for ocean waves. Part I: Definition, calibration and validation. *J. Phys. Oceanogr.*, **40**, 1917–1941, https://doi.org/10.1175/2010JPO4324.1.

——, P. Sutherland, M. Doble, and P. Wadhams, 2016: Ocean waves across the Arctic: Attenuation due to dissipation dominates over scattering for periods longer than 19 s. *Geophys. Res. Lett.*, **43**, 5775–5783, https://doi.org/10.1002/2016GL068204.

Babanin, A. V., 2011: *Breaking and Dissipation of Ocean Surface Waves.* Cambridge University Press, 480 pp.

——, I. R. Young, and M. L. Banner, 2001: Breaking probabilities for dominant surface waves on water of finite constant depth. *J. Geophys. Res.*, **106**, 11 659–11 676, https://doi.org/10.1029/2000JC000215.

——, K. N. Tsagareli, I. R. Young, and D. J. Walker, 2010: Numerical investigation of spectral evolution of wind waves. Part II: Dissipation term and evolution tests. *J. Phys. Oceanogr.*, **40**, 667–683, https://doi.org/10.1175/2009JPO4370.1.

Beitsch, A., L. Kaleschke, and S. Kern, 2014: Investigating high-resolution AMSR2 sea ice concentrations during the February 2013 fracture event in the Beaufort sea. *Remote Sens.*, **6**, 3841–3856, https://doi.org/10.3390/rs6053841.

Bennetts, L. G., and V. A. Squire, 2012: On the calculation of an attenuation coefficient for transects of ice-covered ocean. *Proc. Roy. Soc. London*, **468A**, 136–162, https://doi.org/10.1098/rspa.2011.0155.

——, S. O'Farrell, and P. Uotila, 2017: Impacts of ocean-wave-induced breakup of Antarctic sea ice via thermodynamics in a stand-alone version of the CICE sea-ice model. *Cryosphere*, **11**, 1035–1040, https://doi.org/10.5194/tc-11-1035-2017.

Boutin, G., F. Ardhuin, D. Dumont, C. Sévigny, F. Girard-Ardhuin, and M. Accensi, 2018: Floe size effect on wave-ice interactions: Possible effects, implementation in wave model and evaluation. *J. Geophys. Res. Oceans*, **123**, 4779–4805, https://doi.org/10.1029/2017JC013622.

Cheng, S., and Coauthors, 2017: Calibrating a viscoelastic sea ice model for wave propagation in the arctic fall marginal ice zone. *J. Geophys. Res. Oceans*, **122**, 8770–8793, https://doi.org/10.1002/2017JC013275.

Collins, C. O., and W. E. Rogers, 2017: A source term for wave attenuation by sea ice in WAVEWATCH III: IC4. Tech. Rep. NRL/MR/7320–17-9726, 25 pp., https://www7320.nrlssc.navy.mil/pubs/2017/rogers-2017.pdf.

——, ——, A. Marchenko, and A. V. Babanin, 2015: In situ measurements of an energetic wave event in the Arctic marginal ice zone. *Geophys. Res. Lett.*, **42**, 1863–1870, https://doi.org/10.1002/2015GL063063.

——, ——, and B. Lund, 2016: An investigation into the dispersion of ocean surface waves in sea ice. *Ocean Dyn.*, **63**, 263–280, https://doi.org/10.1007/s10236-016-1021-4

——, M. Doble, B. Lund, and M. Smith, 2018: Observations of surface wave dispersion in the marginal ice zone. *J. Geophys. Res. Oceans*, **123**, 3336–3354, https://doi.org/10.1029/2018JC013788.

De Carolis, G., and D. Desiderio, 2002: Dispersion and attenuation of gravity waves in ice: A two-layer viscous fluid model with experimental data validation. *Phys. Lett.*, **305A**, 399–412, https://doi.org/10.1016/S0375-9601(02)01503-7.

Doble, M. J., and J. R. Bidlot, 2013: Wave buoy measurements at the Antarctic sea ice edge compared with an enhanced ECMWF WAM: Progress towards global waves-in-ice modelling. *Ocean Modell.*, **70**, 166–173, https://doi.org/10.1016/j.ocemod.2013.05.012.

——, G. D. Carolis, M. H. Meylan, J.-R. Bidlot, and P. Wadhams, 2015: Relating wave attenuation to pancake ice thickness, using field measurements and model results. *Geophys. Res. Lett.*, **42**, 4473–4481, https://doi.org/10.1002/2015GL063628.

Donelan, M. A., J. Hamilton, and W. Hui, 1985: Directional spectra of wind-generated ocean waves. *Philos. Trans. Roy. Soc. London*, **315A**, 509–562, https://doi.org/10.1098/rsta.1985.0054.

——, A. V. Babanin, I. R. Young, and M. L. Banner, 2006: Wave-follower field measurements of the wind-input spectral function. Part II: Parameterization of the wind input. *J. Phys. Oceanogr.*, **36**, 1672–1689, https://doi.org/10.1175/JPO2933.1.

Dumont, D., A. Kohout, and L. Bertino, 2011: A wave-based model for the marginal ice zone including a floe breaking parameterization. *J. Geophys. Res.*, **116**, C04001, https://doi.org/10.1029/2010JC006682.

Fox, C., and V. A. Squire, 1990: Reflection and transmission characteristics at the edge of shore fast sea ice. *J. Geophys. Res.*, **95**, 11629, https://doi.org/10.1029/JC095iC07p11629.

——, and ——, 1994: On the oblique reflexion and transmission of ocean waves at shore fast sea ice. *Philos. Trans. Roy. Soc. London*, **347A**, 185–218, https://doi.org/10.1098/rsta.1994.0044.

Hasselmann, K., 1962: On the non-linear energy transfer in a gravity-wave spectrum. Part I: General theory. *J. Fluid Mech.*, **12**, 481–500, https://doi.org/10.1017/S0022112062000373.

——, and Coauthors, 1973: Measurements of wind-wave growth and swell decay during the Joint North Sea Wave Project (JONSWAP). Tech. Rep., Deutches Hydrographisches Institut, Hamburg, Germany, 93 pp., http://resolver.tudelft.nl/uuid:f204e188-13b9-49d8-a6dc-4fb7c20562fc.

Hasselmann, S., K. Hasselmann, J. H. Allender, and T. P. Barnett, 1985: Computations and parameterizations of the nonlinear energy transfer in a gravity-wave Specturm. Part II: Parameterizations of the nonlinear energy transfer for application in wave models. *J. Phys. Oceanogr.*, **15**, 1378–1391, https://doi.org/10.1175/1520-0485(1985)015<1378:CAPOTN>2.0.CO;2.

Hogan, T. F., and Coauthors, 2014: The Navy Global Environmental Model. *Oceanography*, **27**, 116–125, https://doi.org/10.5670/oceanog.2014.73.

Holthuijsen, L. H., 2007: *Waves in Oceaninc and Coastal Waters*. Cambridge University Press, 387 pp.

Huntemann, M., G. Heygster, L. Kaleschke, T. Krumpen, M. Mäkynen, and M. Drusch, 2014: Empirical sea ice thickness retrieval during the freeze up period from smos high incident angle observations. *Cryosphere*, **8**, 439–451, https://doi.org/10.5194/tc-8-439-2014.

Kahma, K. K., and C. J. Calkoen, 1992: Reconciling discrepancies in the observed growth of wind-generated waves. *J. Phys. Oceanogr.*, **22**, 1389–1405, https://doi.org/10.1175/1520-0485(1992)022<1389:RDITOG>2.0.CO;2.

Kaleschke, L., and S. Kern, 2006: Sea-ice concentration for Arctic & Antarctic (ASI-SSMI). Universität Hamburg, accessed 30 April 2020, http://icdc.cen.uni-hamburg.de/1/daten/cryosphere/seaiceconcentration-asi-ssmi.html.

——, and X. Tian-Kunze, 2016: AMSR2 ASI 3.125 km sea ice concentration data, v0.1. Universität Hamburg, accessed 30 April 2020, ftp://ftp-projects.cen.uni-hamburg.de/seaice/AMSR2/3.125km/.

Keller, J. B., 1998: Gravity waves on ice-covered water. *J. Geophys. Res.*, **103**, 7663–7669, https://doi.org/10.1029/97JC02966.

Kohout, A. L., and M. H. Meylan, 2008: An elastic plate model for wave attenuation and ice floe breaking in the marginal ice zone. *J. Geophys. Res.*, **113**, C09016, https://doi.org/10.1029/2007JC004434.

——, and M. J. M. Williams, 2015: Waves in-ice observations made during the SIPEX II voyage of the Aurora Australis, 2012. Australian Antarctic Data Centre, accessed 30 April 2020, https://doi.org/10.4225/15/53266BEC9607F.

——, M. H. Meylan, and D. R. Plew, 2011: Wave attenuation in a marginal ice zone due to the bottom roughness of ice floes. *Ann. Glaciol.*, **52**, 118–122, https://doi.org/10.3189/172756411795931525.

——, M. J. M. Williams, S. M. Dean, and M. H. Meylan, 2014: Storm-induced sea-ice breakup and the implications for ice extent. *Nature*, **509**, 604–607, https://doi.org/10.1038/nature13262.

——, ——, T. Toyota, J. Lieser, and J. Hutchings, 2016: In situ observations of wave-induced sea ice breakup. *Deep-Sea Res. II*, **131**, 22–27, https://doi.org/10.1016/j.dsr2.2015.06.010.

Li, J., A. L. Kohout, and H. H. Shen, 2015: Comparison of wave propagation through ice covers in calm and storm conditions. *Geophys. Res. Lett.*, **42**, 5935–5941, https://doi.org/10.1002/2015GL064715.

——, ——, M. J. Doble, P. Wadhams, C. Guan, and H. H. Shen, 2017: Rollover of apparent wave attenuation in ice covered seas. *J. Geophys. Res. Oceans*, **122**, 8557–8566, https://doi.org/10.1002/2017JC012978.

Li, J.-G., 2012: Propagation of ocean surface waves on a spherical multiple-cell grid. *J. Comput. Phys.*, **231**, 8262–8277, https://doi.org/10.1016/j.jcp.2012.08.007.

Liu, A. K., and E. Mollo-Christensen, 1988: Wave propagation in a solid ice pack. *J. Phys. Oceanogr.*, **18**, 1702–1712, https://doi.org/10.1175/1520-0485(1988)018<1702:WPIASI>2.0.CO;2.

——, B. Holt, and P. W. Vachon, 1991: Wave propagation in the marginal ice zone: Model predictions and comparisons with buoy and synthetic aperture radar data. *J. Geophys. Res.*, **96**, 4605–4621, https://doi.org/10.1029/90JC02267.

Liu, Q., A. V. Babanin, C. Guan, S. Zieger, J. Sun, and Y. Jia, 2016a: Calibration and validation of HY-2 altimeter wave height. *J. Atmos. Oceanic Technol.*, **33**, 919–936, https://doi.org/10.1175/JTECH-D-15-0219.1.

——, ——, S. Zieger, I. R. Young, and C. Guan, 2016b: Wind and wave climate in the Arctic Ocean as observed by altimeters. *J. Climate*, **29**, 7957–7975, https://doi.org/10.1175/JCLI-D-16-0219.1.

——, W. E. Rogers, A. V. Babanin, I. R. Young, L. Romero, S. Zieger, F. Qiao, and C. Guan, 2019: Observation-based source terms in the third-generation wave model wavewatch III: Updates and verification. *J. Phys. Oceanogr.*, **49**, 489–517, https://doi.org/10.1175/JPO-D-18-0137.1.

Maslanik, J., J. Stroeve, C. Fowler, and W. Emery, 2011: Distribution and trends in Arctic sea ice age through spring 2011. *Geophys. Res. Lett.*, **38**, L13502, https://doi.org/10.1029/2011GL047735.

Masson, D., and P. H. Leblond, 1989: Spectral evolution of wind-generated surface gravity waves in a dispersed ice field. *J. Fluid Mech.*, **202**, 43–81, https://doi.org/10.1017/S0022112089001096.

Meylan, M. H., and V. A. Squire, 1996: Response of a circular ice floe to ocean waves. *J. Geophys. Res.*, **101**, 8869–8884, https://doi.org/10.1029/95JC03706.

——, and D. Masson, 2006: A linear Boltzmann equation to model wave scattering in the marginal ice zone. *Ocean Modell.*, **11**, 417–427, https://doi.org/10.1016/j.ocemod.2004.12.008.

——, V. A. Squire, and C. Fox, 1997: Toward realism in modeling ocean wave behavior in marginal ice zones. *J. Geophys. Res.*, **102**, 22 981–22 991, https://doi.org/10.1029/97JC01453.

——, L. G. Bennetts, and A. L. Kohout, 2014: In situ measurements and analysis of ocean waves in the Antarctic marginal ice zone. *Geophys. Res. Lett.*, **41**, 5046–5051, https://doi.org/10.1002/2014GL060809.

——, L. Bennetts, J. Mosig, W. Rogers, M. Doble, and M. Peter, 2018: Dispersion relations, power laws, and energy loss for waves in the marginal ice zone. *J. Geophys. Res. Oceans*, **123**, 3322–3335, https://doi.org/10.1002/2018JC013776.

Montiel, F., V. A. Squire, and L. G. Bennetts, 2016: Attenuation and directional spreading of ocean wave spectra in the

marginal ice zone. *J. Fluid Mech.*, **790**, 492–522, https://doi.org/10.1017/jfm.2016.21.

——, V. Squire, M. Doble, J. Thomson, and P. Wadhams, 2018: Attenuation and directional spreading of ocean waves during a storm event in the autumn Beaufort sea marginal ice zone. *J. Geophys. Res. Oceans*, **123**, 5912–5932, https://doi.org/10.1029/2018JC013763.

Mosig, J. E. M., F. Montiel, and V. A. Squire, 2015: Comparison of viscoelastic-type models for ocean wave attenuation in ice-covered seas. *J. Geophys. Res. Oceans*, **120**, 6072–6090, https://doi.org/10.1002/2015JC010881.

Overland, J. E., and M. Wang, 2013: When will the summer Arctic be nearly sea ice free? *Geophys. Res. Lett.*, **40**, 2097–2101, https://doi.org/10.1002/grl.50316.

Perrie, W., and Y. Hu, 1996: Air–ice–ocean momentum exchange. Part I: Energy transfer between waves and ice floes. *J. Phys. Oceanogr.*, **26**, 1705–1720, https://doi.org/10.1175/1520-0485(1996)026<1705:AMEPTB>2.0.CO;2.

Polnikov, V. G., and I. V. Lavrenov, 2007: Calculation of the nonlinear energy transfer through the wave spectrum at the sea surface covered with broken ice. *Oceanology*, **47**, 334–343, https://doi.org/10.1134/S0001437007030058.

Rabault, J., G. Sutherland, A. Jensen, K. H. Christensen, and A. Marchenko, 2019: Experiments on wave propagation in grease ice: Combined wave gauges and particle image velocimetry measurements. *J. Fluid Mech.*, **864**, 876–898, https://doi.org/10.1017/jfm.2019.16.

Ricker, R., S. Hendricks, L. Kaleschke, X. Tian-Kunze, J. King, and C. Haas, 2017: A weekly Arctic sea-ice thickness data record from merged CryoSat-2 and SMOS satellite data. *Cryosphere*, **11**, 1607–1623, https://doi.org/10.5194/tc-11-1607-2017.

Robinson, N., and S. Palmer, 1990: A modal analysis of a rectangular plate floating on an incompressible liquid. *J. Sound Vibrat.*, **142**, 453–460, https://doi.org/10.1016/0022-460X(90)90661-I.

Rogers, W. E., and D. W. Wang, 2007: Directional validation of wave predictions. *J. Atmos. Oceanic Technol.*, **24**, 504–520, https://doi.org/10.1175/JTECH1990.1.

——, and T. J. Campbell, 2009: Implementation of curvilinear coordinate system in the WAVEWATCH III model. Tech. Rep. NRL/MR/7320–09-9193, Naval Research Laboratory, 42 pp., https://www7320.nrlssc.navy.mil/pubs/2009/rogers1-2009.pdf.

——, and M. D. Orzech, 2013: Implementation and testing of ice and mud source functions in WAVEWATCH III. Tech. Rep. NRL/MR/7320–13-9462, Naval Research Laboratory, 25 pp., https://www7320.nrlssc.navy.mil/pubs/2013/rogers2-2013.pdf.

——, and S. Zieger, 2014: New wave-ice interaction physics in WAVEWATCH III. *22nd IAHR Int. Symp. on Ice*, Singapore, International Association of Hydro-Environment Engineering and Research, 8 pp., https://apps.dtic.mil/dtic/tr/fulltext/u2/a607695.pdf.

——, J. Thomson, H. H. Shen, M. J. Doble, P. Wadhams, and S. Cheng, 2016: Dissipation of wind waves by pancake and frazil ice in the autumn beaufort sea. *J. Geophys. Res. Oceans*, **121**, 7991–8007, https://doi.org/10.1002/2016JC012251.

——, M. Meylan, and A. L. Kohout, 2018a: Frequency distribution of dissipation of energy of ocean waves by sea ice using data from Wave Array 3 of the ONR "Sea State" field experiment. Tech. Rep., Naval Research Laboratory, 28 pp., https://www7320.nrlssc.navy.mil/pubs/2018/rogers2-2018.pdf.

——, P. Posey, L. Li, and R. Allard, 2018b: Forecasting and hindcasting waves in and near the marginal ice zone: Wave modeling and the ONR "Sea State" Field Experiment. Tech. Rep.

NRL/MR/7320–18-9786, Naval Research Laboratory, 164 pp., https://www7320.nrlssc.navy.mil/pubs/2018/rogers-2018.pdf.

Saha, S., and Coauthors, 2014: The NCEP Climate Forecast System version 2. *J. Climate*, **27**, 2185–2208, https://doi.org/10.1175/JCLI-D-12-00823.1.

Skene, D., L. Bennetts, M. Meylan, and A. Toffoli, 2015: Modelling water wave overwash of a thin floating plate. *J. Fluid Mech.*, **777**, R3, https://doi.org/10.1017/jfm.2015.378.

Smith, M., and Coauthors, 2018: Episodic reversal of autumn ice advance caused by release of ocean heat in the Beaufort sea. *J. Geophys. Res. Oceans*, **123**, 3164–3185, https://doi.org/10.1002/2018JC013764.

Squire, V. A., 2007: Of ocean waves and sea-ice revisited. *Cold Reg. Sci. Technol.*, **49**, 110–133, https://doi.org/10.1016/j.coldregions.2007.04.007.

——, 2020: Ocean wave interactions with sea ice: A 2019 reappraisal. *Annu. Rev. Fluid Mech.*, **52**, 37–60, https://doi.org/10.1146/annurev-fluid-010719-060301.

——, and F. Montiel, 2016: Evolution of directional wave spectra in the marginal ice zone: A new model tested with Legacy data. *J. Phys. Oceanogr.*, **46**, 3121–3137, https://doi.org/10.1175/JPO-D-16-0118.1.

——, J. P. Duggan, P. Wadhams, P. J. Rottier, and A. J. Liu, 1995: Of ocean waves and sea ice. *Annu. Rev. Fluid Mech.*, **27**, 115–168, https://doi.org/10.1146/annurev.fl.27.010195.000555.

——, G. L. Vaughan, and L. G. Bennetts, 2009: Ocean surface wave evolvement in the Arctic Basin. *Geophys. Res. Lett.*, **36**, L22502, https://doi.org/10.1029/2009GL040676.

Sutherland, G., and J. Rabault, 2016: Observations of wave dispersion and attenuation in landfast ice. *J. Geophys. Res. Oceans*, **121**, 1984–1997, https://doi.org/10.1002/2015JC011446.

Sutherland, P., and J.-C. Gascard, 2016: Airborne remote sensing of ocean wave directional wavenumber spectra in the marginal ice zone. *Geophys. Res. Lett.*, **43**, 5151–5159, https://doi.org/10.1002/2016GL067713.

——, J. Brozena, W. E. Rogers, M. Doble, and P. Wadhams, 2018: Airborne remote sensing of wave propagation in the marginal ice zone. *J. Geophys. Res. Oceans*, **123**, 4132–4152, https://doi.org/10.1029/2018JC013785.

Thomson, J., 2012: Wave breaking dissipation observed with "SWIFT" drifters. *J. Atmos. Oceanic Technol.*, **29**, 1866–1882, https://doi.org/10.1175/JTECH-D-12-00018.1.

——, and W. E. Rogers, 2014: Swell and sea in the emerging Arctic Ocean. *Geophys. Res. Lett.*, **41**, 3136–3140, https://doi.org/10.1002/2014GL059983.

——, and Coauthors, 2016: Emerging trends in the sea state of the Beaufort and Chukchi seas. *Ocean Modell.*, **105**, 1–12, https://doi.org/10.1016/j.ocemod.2016.02.009.

——, and Coauthors, 2018: Overview of the arctic sea state and boundary layer physics program. *J. Geophys. Res. Oceans*, **123**, 8674–8687, https://doi.org/10.1002/2018JC013766.

Toffoli, A., L. G. Bennetts, M. H. Meylan, C. Cavaliere, A. Alberello, J. Elsnab, and J. P. Monty, 2015: Sea ice floes dissipate the energy of steep ocean waves. *Geophys. Res. Lett.*, **42**, 8547–8554, https://doi.org/10.1002/2015GL065937.

Tolman, H. L., 2003: Treatment of unresolved islands and ice in wind wave models. *Ocean Modell.*, **5**, 219–231, https://doi.org/10.1016/S1463-5003(02)00040-9.

——, 2010: Optimum discrete interaction approximations for wind waves. Part 4: Parameter optimization. Tech. Rep. 288, NOAA/NWS/NCEP/MMAB, 175 pp.

Toyota, T., A. Kohout, and A. D. Fraser, 2016: Formation processes of sea ice floe size distribution in the interior pack

and its relationship to the marginal ice zone off East Antarctica. *Deep-Sea Res. II*, **131**, 28–40, https://doi.org/10.1016/j.dsr2.2015.10.003.

Voermans, J., A. Babanin, J. Thomson, M. Smith, and H. Shen, 2019: Wave attenuation by sea ice turbulence. *Geophys. Res. Lett.*, **46**, 6796–6803, https://doi.org/10.1029/2019GL082945.

Wadhams, P., 1973: Attenuation of swell by sea ice. *J. Geophys. Res.*, **78**, 3552–3563, https://doi.org/10.1029/JC078i018p03552.

——, 1981: The ice cover in the Greenland and Norwegian seas. *Rev. Geophys.*, **19**, 345–393, https://doi.org/10.1029/RG019i003p00345.

——, and J. Thomson, 2015: The Arctic Ocean cruise of R/V Sikuliaq 2015, an investigation of waves and the advancing ice edge. *Il Polo*, **70**, 9–38.

——, V. A. Squire, J. A. Ewing, and R. W. Pascal, 1986: The effect of the marginal ice zone on the directional wave spectrum of the ocean. *J. Phys. Oceanogr.*, **16**, 358–376, https://doi.org/10.1175/1520-0485(1986)016<0358:TEOTMI>2.0.CO;2.

Wang, R., and H. H. Shen, 2010: Gravity waves propagating into an ice-covered ocean: A viscoelastic model. *J. Geophys. Res.*, **115**, C06024, https://doi.org/10.1029/2009JC005591.

Williams, T. D., L. G. Bennetts, V. A. Squire, D. Dumont, and L. Bertino, 2013a: Wave-ice interactions in the marginal ice zone. Part I: Theoretical foundations. *Ocean Modell.*, **71**, 81–91, https://doi.org/10.1016/j.ocemod.2013.05.010.

——, ——, ——, ——, and ——, 2013b: Wave-ice interactions in the marginal ice zone. Part 2: Numerical implementation and sensitivity studies along 1D transects of the ocean surface. *Ocean Modell.*, **71**, 92–101, https://doi.org/10.1016/j.ocemod.2013.05.011.

——, P. Rampal, and S. Bouillon, 2017: Wave–ice interactions in the nextsim sea-ice model. *Cryosphere*, **11**, 2117–2135, https://doi.org/10.5194/tc-11-2117-2017.

WW3DG, 2019: User manual and system documentation of WAVEWATCH III version 6.07. Tech. Note 333, NOAA/NWS/NCEP/MMAB, 465 pp., https://github.com/NOAA-EMC/WW3/wiki/Manual.

Young, I. R., 1999: *Wind Generated Ocean Waves*. Elsevier Science Ltd., 287 pp.

——, and G. P. van Vledder, 1993: A review of the central role of nonlinear interactions in wind-wave evolution. *Philos. Trans. Roy. Soc. London*, **342A**, 505–524.

Zhao, X., and H. Shen, 2016: A diffusion approximation for ocean wave scatterings by randomly distributed ice floes. *Ocean Modell.*, **107**, 21–27, https://doi.org/10.1016/j.ocemod.2016.09.014.